Article

Cell-cycle-linked growth reprogramming encodes developmental time into leaf morphogenesis

Graphical abstract
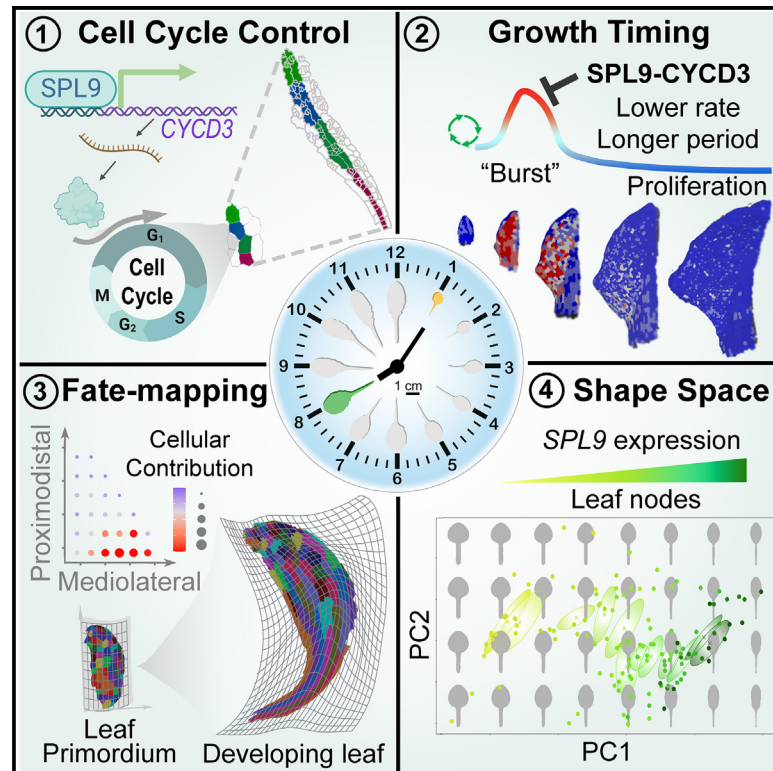
Authors

Xin-Min Li, Hannah Jenke,
Sören Strauss, ..., Richard S. Smith,
Adam Runions, Miltos Tsiantis

Correspondence

tsiantis@mpipz.mpg.de

In brief

Li et al. study cellular growth reprogramming underlying heteroblastic changes in leaf form. They show that an SPL9-CYCD3 transcriptional module encodes developmental time into leaf morphogenesis by timing cell proliferation and growth, thus orchestrating plant development across temporal scales, from the cell cycle to age-dependent organ form.

Highlights

- Time-lapse and fate maps yield a cellular growth framework for leaf heteroblasty

- A default "cell proliferation burst" underpins juvenile leaf morphogenesis

- SPL9 maintains proliferative growth along an age-dependent proximodistal gradient

- SPL9-CYCD3 transcriptional module times leaf development via cell cycle control

CellPress

Article

Cell-cycle-linked growth reprogramming encodes developmental time into leaf morphogenesis

Xin-Min Li,[1] Hannah Jenke,[1] Sören Strauss,[1] Christos Bazakos,[1,3] Gabriella Mosca,[1,4] Rena Lymbouridou,[1]
Daniel Kierzkowski,[1,5] Ulla Neumann,[2] Purva Naik,[1] Peter Huijser,[1] Stefan Laurent,[1,6] Richard S. Smith,[1,7]
Adam Runions,[1,8] and Miltos Tsiantis[1,9,*]

[1]Department of Comparative Development and Genetics, Max Planck Institute for Plant Breeding Research, Carl-von-Linné Weg 10, 50829
Cologne, Germany
[2]Central Microscopy (CeMic), Max Planck Institute for Plant Breeding Research, Carl-von-Linné Weg 10, 50829 Cologne, Germany
[3]Present address: Institute of Plant Breeding and Genetic Resources, ELGO-DIMITRA, Thermi, Thessaloniki 57001, Greece
[4]Present address: Center for Plant Molecular Biology, University of Tübingen, Auf Der Morgenstelle 32, 72076 Tübingen, Germany
[5]Present address: Institut de Recherche en Biologie Végétale, Département de Sciences Biologiques, Université de Montréal, 4101
Sherbrooke St E, Montréal, QC H1X 2B2, Canada
[6]Present address: BioNTech SE, An der Goldgrube 12, 55131 Mainz, Germany
[7]Present address: John Innes Centre, Norwich Research Park, Norwich NR4 7UH, UK
[8]Present address: Department of Computer Science, University of Calgary, Calgary, AB T2N 1N4, Canada
[9]Lead contact
*Correspondence: tsiantis@mpipz.mpg.de
https://doi.org/10.1016/j.cub.2023.12.050

SUMMARY

How is time encoded into organ growth and morphogenesis? We address this question by investigating hetero-blasty, where leaf development and form are modified with progressing plant age. By combining morpho-metric analyses, fate-mapping through live-imaging, computational analyses, and genetics, we identify age-dependent changes in cell-cycle-associated growth and histogenesis that underpin leaf heteroblasty. We show that in juvenile leaves, cell proliferation competence is rapidly released in a "proliferation burst" coupled with fast growth, whereas in adult leaves, proliferative growth is sustained for longer and at a slower rate. These effects are mediated by the SPL9 transcription factor in response to inputs from both shoot age and individual leaf maturation along the proximodistal axis. SPL9 acts by activating *CyclinD3* family genes, which are sufficient to bypass the requirement for SPL9 in the control of leaf shape and in heteroblastic reprogramming of cellular growth. In conclusion, we have identified a mechanism that bridges across cell, tissue, and whole-organism scales by linking cell-cycle-associated growth control to age-dependent changes in organ geometry.

INTRODUCTION

Biological development is programmed in space and time, and while studies of morphogenesis have shed considerable light on the spatial control of development in plants and animals,[1,2] the temporal control of development is not as well understood.[3–5] Developmental programs of complex eukaryotes typically unfold over three interlinked temporal scales: that of the cell, which is dominated by cell cycle control; the organ, where cells are recruited into organ buds that grow, differentiate, and acquire their final forms over time; and finally, the whole organism, where the progress of time causes pervasive and coordinated morphological and physiological changes that often relate to the ability to reproduce. Mechanisms that integrate these three facets of temporal control of development (cell, tissue and organ, and whole organism) are unclear. Plant leaves offer an attractive system to study these problems, because many plants produce leaves of different morphologies as their shoots age (a phenomenon known as heteroblasty), and these changes are often linked to reproductive maturation and overall physiology.[6–8]

In both plants and animals, microRNA circuits have been identified as crucial developmental timers.[9,10] In plants, a conserved microRNA, miR156, controls plant aging by targeting several members (11/17 in *Arabidopsis thaliana* Col-0) of a plant-specific transcription factor family named SQUAMOSA PROMOTER BINDING PROTEIN-LIKE (SPL).[11–13] Concomitant with miR156 decline, the expression of these *SPL* genes increases with age and influences both leaf morphology and the time to flower and reproduce.[12,14–17] In *A. thaliana*, the *SPL9* gene is a major driver of the transition from the juvenile to the adult stage, which is mirrored by changes in leaf morphology.[12,16] For example, juvenile leaves lack *SPL9* expression, and they have small and round blades clearly delimited from the basal petiole. Conversely, adult leaves that express *SPL9* have larger oval-shaped leaf blades and show a more gradual delimitation of the blade from the petiole (Figure 1A). *SPL9* acts to promote these morphological transitions redundantly with its paralog *SPL15*, which is also miRNA156 regulated.[18,19] However, there is a division of labor between these genes[12,14,16,17] as *SPL9* plays a more important role in leaf morphogenesis,[16] whereas *SPL15* strongly influences flowering time.[20] Multiple processes

are thought to act downstream of SPLs,[12,14,16,19,21–28] but how exactly SPL9 regulates the amount, direction, and duration of growth and whether its action on leaf shape depends mostly on multiple small-effect genes versus a few major-effect genes remains unclear.

Although many regulators of leaf development have been identified,[29–31] how they organize plant cell growth to yield final leaf forms is only recently beginning to be understood.[32–34] Prior work in *A. thaliana* has shown that differentiation progresses from tip to base[35–37] and that various regulatory modules progressively confine cell proliferation, which is initially primordium wide, to the leaf base.[31,38,39] Although the rate of these proliferation-differentiation transitions can influence leaf form,[37,40] whether and how the timing of this process is relevant to leaf heteroblasty, for example, by affecting the rate or relative duration of mediolateral (ML) versus proximodistal (PD) growth, is unclear. Another potential explanation for heteroblasty is that changes in cellular growth anisotropy between different leaves can alter leaf shape.[24,41,42] However, limited spatiotemporal windows of analysis and a lack of direct comparison between juvenile and adult fate maps and growth patterns[24,32,33,35,37,43,44] have made it difficult to draw solid conclusions about the generative mechanisms of leaf heteroblasty. Notably, a combination of time-lapse imaging and computational modeling demonstrated how regulated growth and proliferation control along the PD axis, together with margin patterning, produces the adult leaf shape of *A. thaliana*, which bears marginal serrations, in contrast to that of its relative *Cardamine hirsuta*, which exhibits slower differentiation and bears complex leaves subdivided into leaflets.[33] Nonetheless, it is still unclear how this cell growth program is tuned as a plant ages to generate heteroblasty, especially in the context of the complex and largely unresolved interplay between cell proliferation and growth.[32]

Here, we report the cell-level growth features that underpin heteroblastic development in *A. thaliana* leaves and elucidate the role of SPL9 in this process. By combining lineage tracing, molecular genetics, and computational analysis, we show that the juvenile and adult leaf morphogenesis programs are characterized by SPL9-dependent differences in the spatiotemporal pattern of proliferative growth and the ability to enter an endoreduplication-associated differentiation program. Specifically, we show that proliferation potential in juvenile leaves is rapidly extinguished in a "proliferation burst" linked to fast growth but is sustained by SPL9 in adult leaves. We further show that *CYCD3* genes of the G1 phase cyclin D family, as transcriptional targets of SPL9, are sufficient to bypass the requirement for SPL9 in leaf morphogenesis by maintaining cell proliferation competence. This SPL9-CYCD3 transcriptional module yields the different geometries of juvenile and adult leaves, in response to temporal inputs from shoot age and leaf maturation. Overall, we conceptualize how SPL9 action links the temporal control of cell, tissue, and whole-shoot biology to shape heteroblastic development.

RESULTS

Divergent cellular growth patterns underpin leaf heteroblasty

To understand the cellular growth regulation underlying the juvenile-to-adult shape transition in *A. thaliana* leaves (Figure 1A), we performed time-lapse imaging to compare the early development (1–6 days after initiation [DAI]) of Col-0 leaf1 (juvenile) and leaf8 (adult) leaves—where the latter can be up to 8 times the area of the former at maturity (Figures 1A and S2E). We then computed full-surface fate maps (Figure 1B; Video S1) and measured the amount, duration, and direction of growth and cell proliferation in these samples (Figures 1C–1J and S1). In doing so, we identified four aspects that mark a juvenile growth pattern compared with the adult one. (1) There is more pronounced cell proliferation at early stages (2–3 DAI) in juvenile leaves, which abruptly stops. This in effect creates a cell proliferation burst while reducing the overall duration of cell proliferation relative to adult leaves (Figures 1D, 1E, S1J1, S1K1, and S1L1; Video S1). (2) There is enhanced areal growth in juvenile leaves, especially in association with the proliferation burst and petiole differentiation (Figures 1G, 1H, S1J2, S1K2, and S1L2; Video S1). (3) Cell expansion progresses from distal to proximal in the leaf blade and along the leaf margin and the midrib-petiole region in both juvenile and adult leaf development, whereas this progression is accelerated in juvenile leaves (Figures 1C, 1F, S1A–S1C, S1J3, S1K3, and S1L3). (4) Consistent with the higher PD than ML growth in juvenile leaves (Figures 1J, S1E–S1I, S1J4–S1J6, and S1K4–S1K6), growth anisotropy is strongly elevated at the primordium base compared with adult leaves (Figures 1I, S1D, S1J7, S1K7, and S1L4).

Because the proliferation burst we documented in juvenile leaves at 2–3 DAI is a distinctive feature of juvenile leaf development not seen in adult leaves, we fate-mapped the population of cells undergoing it to better understand its morphogenetic significance. We found that the "burst" population gives rise to the majority of the blade and petiole in Col-0 leaf1, whereas the equivalent cell population in adult leaves makes a more limited contribution to leaf histogenesis (Figures 1K and 1L). This suggests that the proliferation burst has a pivotal role in blade geometry and petiole-blade delimitation, and thereby juvenile leaf form. For a more holistic and unbiased understanding of how the proliferation burst effects heteroblastic growth reprogramming, we developed a two-dimensional (2D) growth-alignment methodology (Figure S1M). We used this to quantitatively compare fate maps, in particular, to examine the histogenic contributions of equivalent cell populations in juvenile versus adult primordia. This analysis showed that a small cell population at the primordium base, which closely overlaps with the "proliferation burst" population, makes a major contribution to leaf1 development from 2 to 5 DAI (Figures 1M and 1N). Contrastingly, the equivalent cells contribute to the adult leaf in a less pronounced fashion, with more distal cells playing a prominent role in leaf8 blade histogenesis (Figures 1O and 1P).

In summary, we have identified age-dependent cellular growth features that distinguish juvenile and adult leaves. We have also demonstrated that cell proliferation competence is released abruptly in leaf1, in the form of a proliferation burst (Figures 1D and 1E). The extinction of proliferation subsequent to this burst likely underlies the reduced total cell number (Figure S2F) and smaller leaf size of leaf1 compared with leaf8 (Figure S2E). Furthermore, after this burst we observe a rapid and relatively synchronous transition from cell proliferation to cell expansion (Figures S1A–S1C). Consistent with previous leaf growth models,[33,34] we hypothesize that this premature cell expansion,
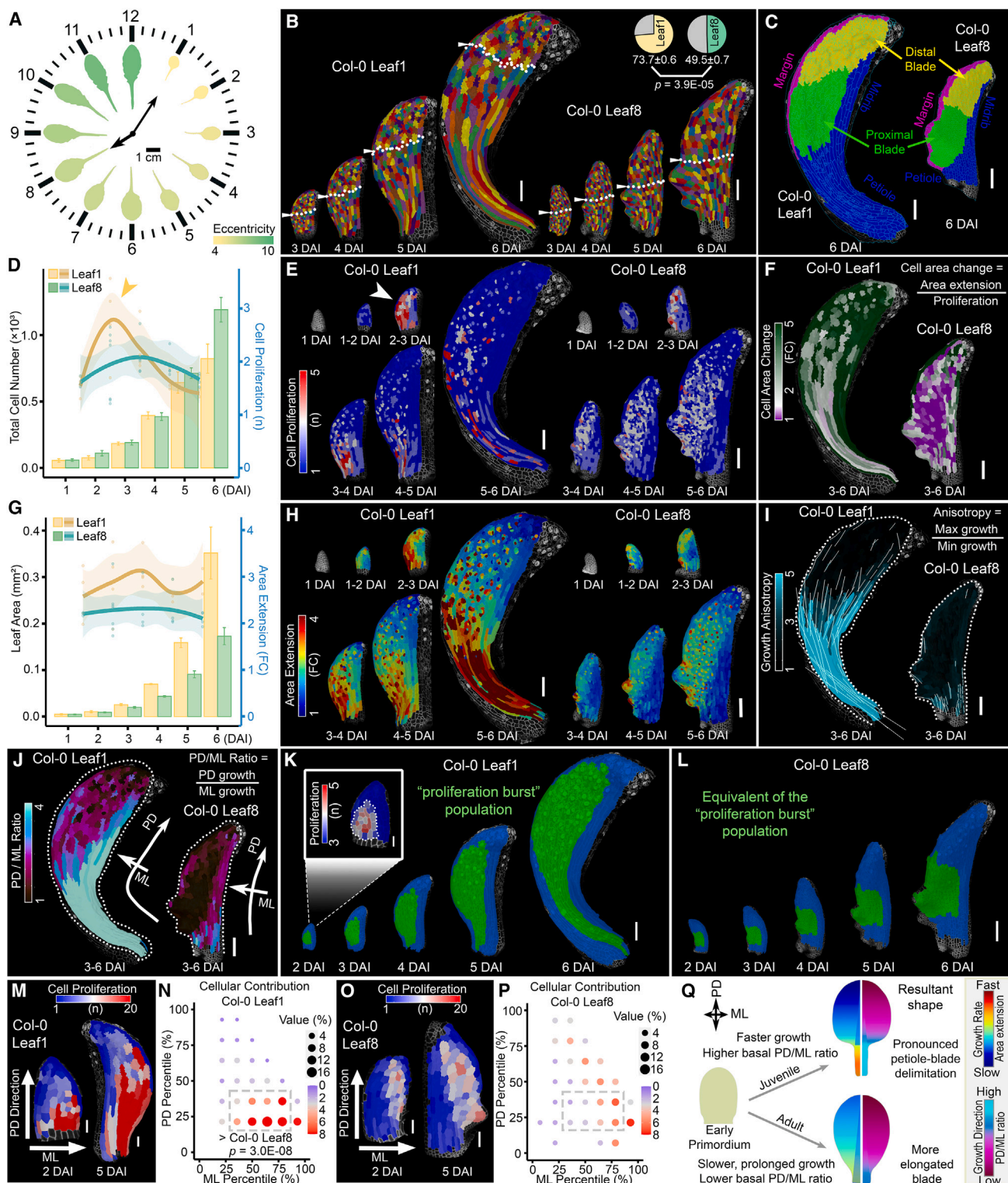
Figure 1. Cellular growth patterns in *A. thaliana* juvenile versus adult leaves

(A) Clockface depicting age-dependent geometric changes of Col-0 mature leaves 1–12. Leaf1 and leaf8 are indicated by clock hands as representatives of juvenile and adult leaves, respectively. Leaf color shows mean shape eccentricity, n = 10.

(B) Cell fate maps for Col-0 leaf1 and leaf8. Cells at 3 days after initiation (DAI) and their progeny clones are color coded. White triangles and dashed lines track the 3 DAI proximodistal (PD) midline. Pie charts show the areal contribution (%) of the 3 DAI proximal (colored) and distal (gray) halves to 6 DAI leaves. Below, mean ± SE of proximal contributions. p, Welch's t test.

(legend continued on next page)

when coupled with strongly anisotropic growth of the base (Figures 1I, 1J, and S1D–S1I), likely accounts for the pronounced petiole elongation and blade-petiole demarcation in juvenile leaves (Figures 1Q and S1N). Contrastingly, proliferation in leaf8 is slower and more sustained (Figures 1D and 1E). It is associated with a gradual basipetal progression of cell expansion (Figures S1A–S1C) and reduced anisotropic growth at the base (Figures 1I, 1J, and S1D–S1I), which likely contributes to the more elongated adult leaf with the blade blending more gradually into the less prominent petiole (Figures 1Q and S1O). Overall, these observations highlight how the progression of plant age changes cell growth and proliferation (Figures 1D–1J), and the histogenic potential of equivalent cell tiers within the immature leaf bud (Figures 1B and 1K–1P), to result in heteroblasty.

SPL9 sustains cell proliferation during leaf heteroblastic growth reprogramming

To investigate leaf heteroblasty and its genetic control quantitatively, we performed a principal-component analysis (PCA)-based multivariate analysis[45] of Col-0 leaf shape changes in response to shoot aging and *SPL9* genetic perturbations (Figure 2A). The first principal component (PC1) from this shape analysis accounted for a substantive amount (>80%) of shape variation including blade roundness and petiole delimitation and highly correlated with shoot age in wild-type Col-0 (Figure 2A). Thus, PC1 emerged as a good quantitative metric for heteroblasty. We found that *SPL9* is necessary and sufficient for both heteroblastic changes in mature leaf shape as captured by PC1 (Figures 2A and S2D) and associated regulation of leaf area and cell number (Figures S2E and S2F). SPL9 also affects the leaf initiation rate (plastochron length,[19] Figures S2A and S2B), but its action on leaf morphogenesis is likely to be, at least in part, genetically separable because (1) *pSPL9::SPL9r:Venus* (miR156-*resistant SPL9* allele[14,16,19]) can accelerate heteroblastic changes in leaf shape compared with both wild-type leaves of the same leaf nodes and leaves that formed at the same chronological time (Figures 2A and S2A–S2D), and (2) *SPL9* complemented the heteroblastic delay of the *spl9spl15* mutant more effectively than the plastochron defect (Figures 2A and S2A–S2D).

To examine how SPL9 modulates cellular growth pattern to alter leaf geometry with age, we live-imaged the growth of

SPL9 loss-of-function (*spl9spl15*) leaf8 and gain-of-function (*pSPL9::SPL9r:Venus*) leaf1. We found that *spl9spl15* "juvenilized" the leaf8 growth pattern with regard to all four of the heteroblastic growth features we identified above, whereas *pSPL9::SPL9r:Venus* transformed the leaf1 developmental pattern into a more adult one (Figures 2B–2D, S2G–S2N4, and S3A1–S3F; Videos S2 and S3). Of particular note is the proliferation burst, which is turned off by *pSPL9::SPL9r:Venus* in leaf1 while restored in *spl9spl15* adult leaves (Figures 2B, 2D, and S2N1; Videos S2 and S3). Concomitantly, proliferation lasts longer in *pSPL9::SPL9r:Venus* leaf1 but shorter in *spl9spl15* leaf8, compared with wild-type leaves of the same node (Figures 2B, 2D, S2N1, and S3A1–S3A3). Correspondingly, *pSPL9::SPL9r:Venus* represses the contribution of petiole-lineage cells while enhancing the contribution of blade-lineage cells to leaf development (Figures S2O, S2Q–S2S, and S3G–S3H'), leading to an acropetal shift of the weighted average of growth contribution (Figures 2E and S3K)—and the opposite effect is observed in *spl9spl15* (Figures 2E, 2G, S2P, S2T, S2U, and S3I–S3K). These fate-mapping analyses indicate that SPL9 decelerates the basipetal release of cell proliferation, resulting in a higher histogenic contribution of distal primordium cells, and also help understand the role of SPL9 in retarding petiole delimitation and elongation[21,43] (Figure 1Q).

One way by which SPL9 could antagonize the cell proliferation burst is through slowing down the cell cycle. To test this idea, we measured cell cycle length during the proliferation burst in a 2-h-window time-lapse experiment (Figures S3L and S3M) because this shorter interval allowed for more efficient cell cycle tracking. We observed that the cell cycle ran faster in Col-0 leaf1 cells compared with cells in leaf8 and that it slowed down in response to ectopic *pSPL9::SPL9r:Venus* (Figure 2F), indicating that SPL9 constrains the proliferation rate. Considering that cell division execution is intricately coordinated with cell size control,[46,47] we then examined the coordination between cell area and proliferation underlying the proliferation burst. We found that cells that subsequently undergo the proliferation burst (in Col-0 leaf1 or *spl9spl15* leaf8 blade) are significantly larger than their counterparts that do not (Col-0 leaf8 and *pSPL9::SPL9r:Venus* leaf1, Figure 2H). This finding indicates that SPL9 modulates cell cycle rate and cell size coordinately, thereby promoting smaller-sized, slower-cycling cells. Notably, in the absence of *SPL9* expression,

(C–J) Cellular features of heteroblastic changes in leaf growth. (C) Cell type classification. Cell proliferation (D and E) and growth rate (G and H, area extension in fold change, FC) were tracked from 1 to 6 DAI, cell area change (F) and growth directionality (I, anisotropy; and J, PD/ML ratio, see STAR Methods) from 3 to 6 DAI were quantified. Daily changes in cell proliferation (D) and growth (G) were plotted against total cell number (D) and leaf area (G), respectively. Left y axes, bar plots; error bar, mean ± SE. Right y axes, dot plots with local regressions and 95% confidence intervals (shaded). Arrowheads in (D) and (E), proliferation burst. (K and L) Lineage tracing of the proliferation burst. The cell population experiencing the proliferation burst, corresponding to a higher proliferation rate from 2 to 3 DAI in leaf1 (inset), is fate mapped (in green) until 6 DAI (K). A similarly proportioned cell population at an equivalent position is tracked in the same way in leaf8 (L). (M–P) Spatial distribution of cell proliferation (M and O) and its contribution (N and P). Cell proliferation is projected on both 2 DAI (flipped primordium with organ coordinates corresponding to the axes of the neighboring plot) and 5 DAI meshes (M, leaf1; O, leaf8). Contributions of cells at 2 DAI to cell populations of 5 DAI leaves are aligned along the PD-ML axes (N, leaf1; P, leaf8; see Figure S1M and STAR Methods). The cellular contributions of proximal blade bins (the "proliferation burst" cell population in leaf1, indicated in dashed boxes) were compared by two-way ANOVA.

(Q) Hypothetical conceptual model of the role of regulated growth in heteroblasty. In juvenile leaf primordia (top), where the proliferation burst occurs, growth is faster overall, and higher along the PD relative to the ML axis at the base, resulting in a clearer petiole-blade delimitation. In adult primordia (bottom), growth is slower and more prolonged along a PD gradient, and it shows a less pronounced difference along the PD relative to the ML axis. These features lead to a larger, more elongated leaf blade with a less prominent petiole.

Scale bars: 1 cm (A), 100 μm (B, C, E, F, and H–L), 20 μm for samples at 2 DAI and 50 μm for 5 DAI samples in (M) and (O), 20 μm for the magnified view of the proliferation burst (K, inset). n = 4 biological replicates (B–P), representative heatmaps are shown, with measures between two time points projected on the latter (E, F, and H–J), unless otherwise indicated (K [inset], M, and O).

See also Figures S1, S3, and S7 and Video S1.
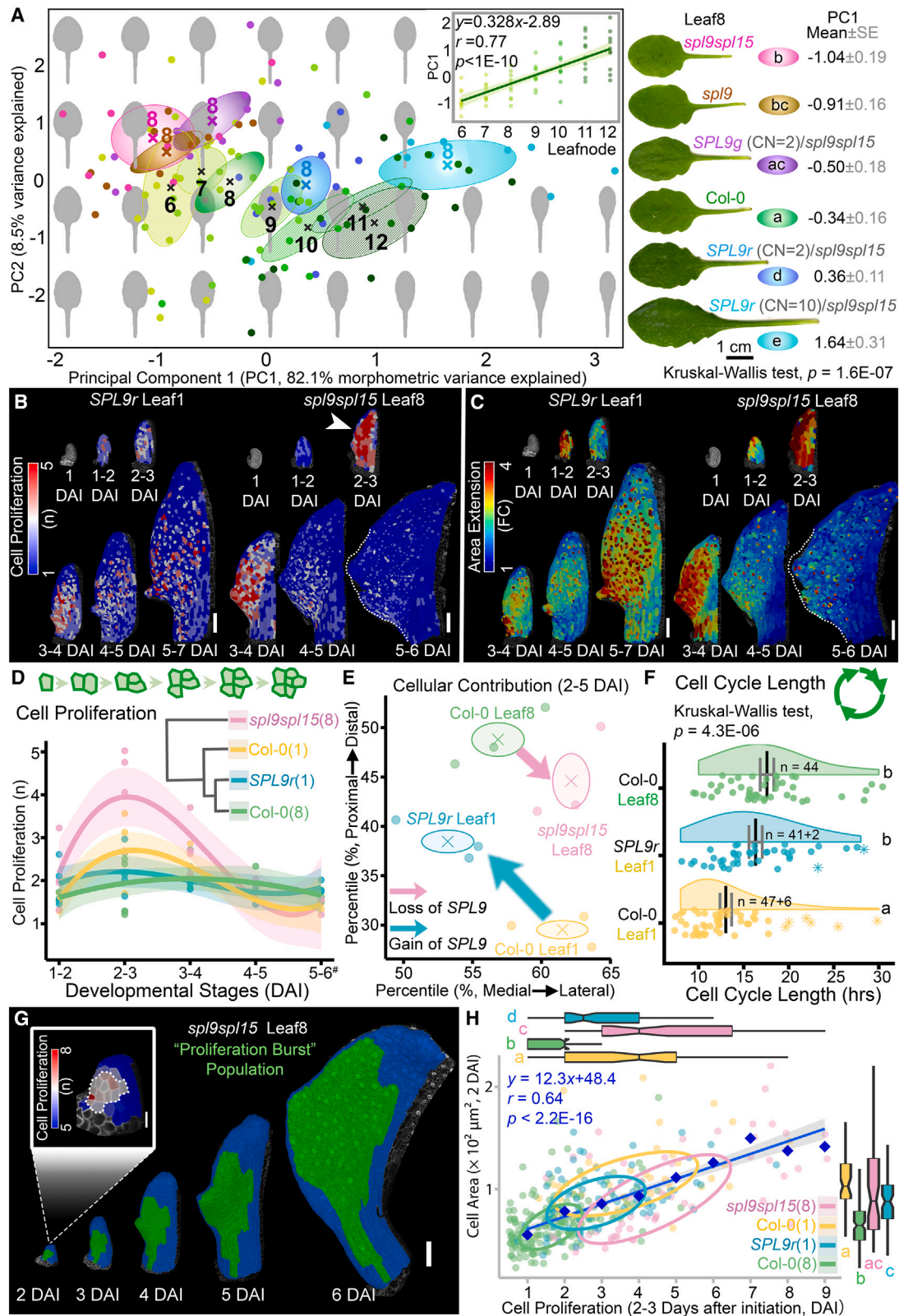
Figure 2. SPL9 modulates heteroblastic growth in association with cell cycle timing

(A) PCA-based shape-space analysis of Col-0 heteroblasty (leaf6–12, numbered) and the effects of SPL9 (leaf8 with differential SPL9). Mean ± SE (crosses in ellipses). Inset, correlation between PC1 and leaf node in Col-0. Leaf8 representatives and color codes are presented on the right. CN, transgene copy number.

(legend continued on next page)

blade areal growth is accelerated concomitant with the proliferation burst, in association with increased cell size (Figure S3N). These observations indicate that the proliferation burst is characterized by distinctive relations of cell growth, cell cycle progression, and cell size because the negative correlation between cell area and growth rate that is otherwise widespread during leaf development is weakened at this stage (Figures S3O–S3Q5).

Together, these findings show how SPL9 reprograms cellular growth to reshape leaves with progressive age. The core logic of this SPL9-regulated timing mechanism involves a developmental trade-off: proliferative growth is restrained early in adult leaf development by SPL9 but persists for longer (Figures 1D–1H and 2B–2D), resulting in a larger leaf with more cells (Figures S2E and S2F). A key feature of this system is that SPL9 temporally modulates a spatially encoded proliferation burst, which in the absence of SPL9 action, leads to rapid cell expansion and thereby the juvenile form. Anisotropy might also follow this trade-off logic, as it is maintained by SPL9 at a relatively low level at the leaf base in early stages (Figures 1I, S1D, S1L4, S2J, S2N4, and S3F), and then increases gradually with the demarcation of the petiole.[24]

SPL9 integrates shoot- and tissue-level temporal information

To examine how the spatiotemporal expression of *SPL9* is linked to its regulation of cellular growth and histogenesis that results in heteroblasty, we studied two different translational reporters, *pSPL9::SPL9:GUS*[12] and *pSPL9::SPL9:Venus*, using histochemical staining and confocal microscopy, respectively. We found that, together with an increase in its expression level,[12] the duration of *SPL9* expression also increases with leaf node progression (shoot age; Figures 3A, S4A, and S4B). At the tissue level, we observed that *SPL9* expression follows a basipetal and lateral decline during leaf8 development (Figure S4A), and further quantification showed that epidermal SPL9 concentration follows this same spatiotemporal pattern (Figures 3A and 3B), which is reminiscent of the spatiotemporal decline in proliferation observed in leaf8 (Figure 1E). This decline in *SPL9* expression along the PD axis is inhibited in the absence of miR156 regulation (e.g., in *pSPL9::SPL9r:Venus/spl9spl15* leaf1, Figures S4B and S4B′), indicating that miR156 plays a role in this progression.

Considering the significance of the epidermis in plant morphogenesis,[33,48,49] we next examined the role of epidermal SPL9 in

heteroblasty. We found that *SPL9r* expression in the leaf epidermis (*pATML1*[50]*::mTFP1:SPL9r*, Figure 3C) was sufficient to accelerate leaf heteroblasty (Figure S4E)—including subepidermal cell growth (Figure S4F)—as was also the case under the *SPL9* native promoter, or a constitutive promoter driving *SPL9r* expression in multiple cell layers (Figures S4C–S4F). Time-lapse analyses further confirmed that *pATML1::mTFP1:SPL9r* converted leaf1 growth to an adult pattern (Figures 3D, 3E, S4G–S4Q′; Video S2), i.e., displaying prolonged blade proliferation (Figure S4J), relatively slow and uniform growth (Figures 3D, S4H, and S4I), retarded cell expansion (Figures 3D and S4K–S4N), repressed anisotropy at the base of the primordium (Figures 3D and S4O), and accordingly, more uniform histogenesis along the PD axis (Figures 3E, S4G, S4H, and S4P–S4Q′).

Taken together, the above findings indicate that *SPL9* responds to the progression of developmental time in two ways: first, with an increase in gene expression as the plant ages and progressive leaf nodes form, and second, with a tissue-level decline during the maturation of individual leaves, which slows as the plant ages. Additionally, our observations suggest that SPL9 action in the epidermis likely has a central role in leaf heteroblasty.

SPL9 impedes the transition from cell proliferation to endoreduplication and differentiation

Our findings suggest that SPL9 sustains cell proliferation to drive the heteroblastic transition of leaf growth patterns. Because the maintenance of proliferation generally leads to the retardation of differentiation, we evaluated the effect of SPL9 on the timing of differentiation using pavement cell geometry (area [Figures 4A–4C] and lobeyness [Figures 4D–4F]) and stomatal emergence (Figures 4G–4I) as indicators of individual cell maturation and tissue differentiation, respectively.[33,42] We observed that the basipetal progression of these measures is repressed by SPL9 in Col-0 leaf8 and *pSPL9::SPL9r:Venus* leaf1 development, resulting in a reduced level of differentiation in response to SPL9 till 5 DAI (Figures 4A–4I). This spatiotemporal suppression of differentiation by SPL9 coincides with its modulation of cell expansion (Figures S1A, S2H, and S4K). These findings, together with its control of petiole differentiation (Figures 1Q, S1N, S1O, S2O, S2P, and S4H), indicate that SPL9 activity retards leaf differentiation and maturation. This slowing down of differentiation,

---

(B and C) Representative heatmaps of cell proliferation (B) and area extension (C). Arrowhead, proliferation burst. DAI, days after initiation. FC, fold change. Scale bars, 100 μm.

(D) Temporal dynamics of cell proliferation. Inset, hierarchical clustering. #, 5–7 DAI for *SPL9r*.

(E) Spatial shift of cellular contributions in response to SPL9. Dot, weighted mean of cellular contribution matrix (see Figures 1N, 1P, S2S, and S2U). Ellipse, defined by standard deviations in both directions; inner cross, mean.

(F) Cell cycle lengths during the proliferation burst. Cloud, data distribution; (∗), guard cell division (showing extended duration, numbers given after the plus sign and included in statistical test); (·), other epidermal cells. Error bar, mean ± SE.

(G) Developmental tracing of the proliferation burst in *spl9spl15* leaf8. A cell population with a relatively higher proliferation rate from 2 to 3 DAI (inset) is tracked (in green) until 6 DAI. Scale bars: 20 μm in the inset and 100 μm for lineage tracing.

(H) Positive correlation between cell area and proliferation during the proliferation burst. Cell proliferation (2–3 DAI) and starting cell area (2 DAI) were plotted and compared among different proximal blade cells. Blue diamonds indicate the average cell area at each proliferation level. Ellipse, standard error. Boxplots summarize cell proliferation (top) and cell area (right) of different genotypes.

SPL9g, *pSPL9::SPL9:Venus*; *SPL9r*, *pSPL9::SPL9r:Venus*. Numbers in brackets, leaf nodes (D and H).

Fitting lines, linear regression (A [inset] and H) or cubic polynomial regression (D); shade, 95% confidence interval. Lowercase letters in (A, F, and H), Wilcoxon rank-sum post hoc test, false discovery rate (FDR) adjusted. n = 10 (A), 3–4 (B–E, G, and H), and as indicated in (F).

See also Figures S2, S3, and S7 and Videos S2 and S3.
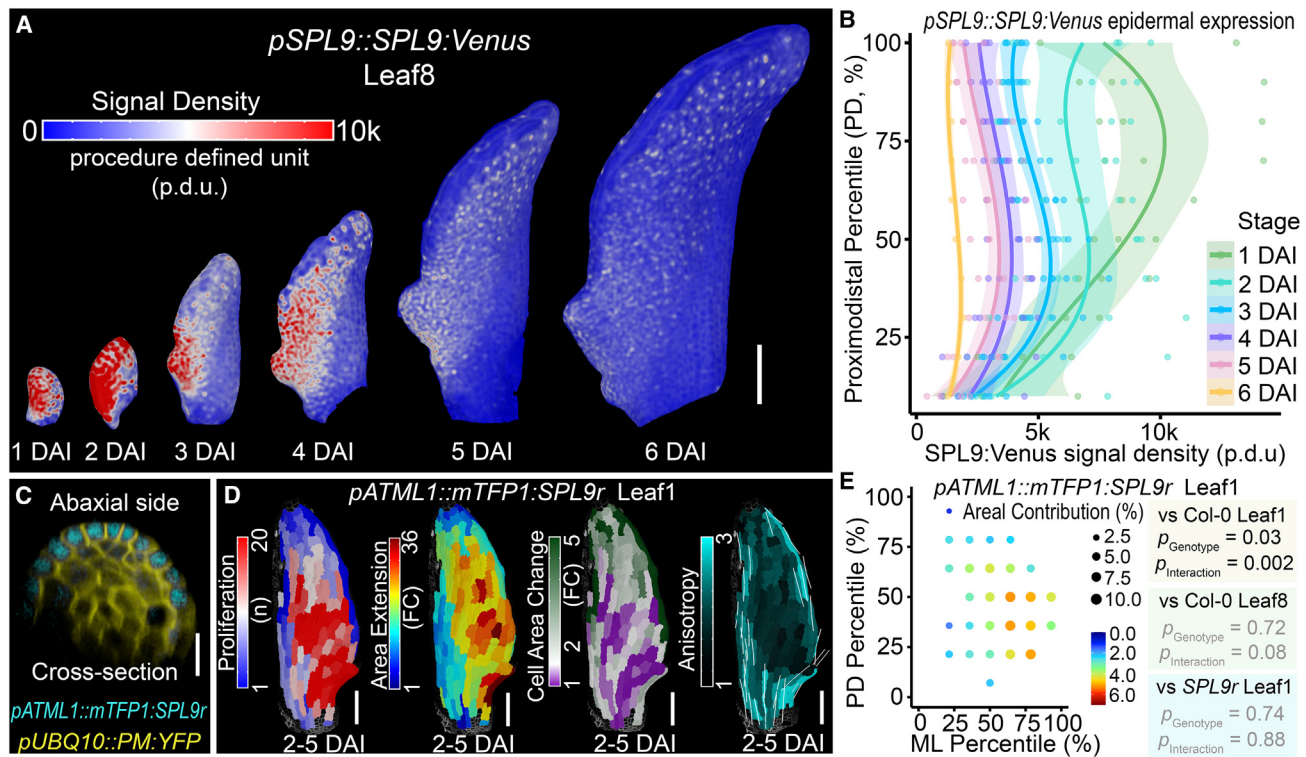
Figure 3. Spatiotemporal inputs into SPL9 action

(A and B) *SPL9* spatiotemporal expression in Col-0 leaf8 development. SPL9 distribution in leaf8 epidermis from 1 to 6 days after initiation (DAI) is visualized as a heatmap, (A) and its density was plotted as a function of the distance from the base (B). Cubic regression with 95% confidence interval (shade).

(C–E) Epidermal SPL9 is sufficient to drive juvenile-adult reprogramming in *pATML1::mTFP1:SPL9r* leaf1. (C) Epidermis-specific expression of miR156-resistant *SPL9* using *pATML1* promoter. (D) Representative growth heatmaps from 2 to 5 DAI. FC, fold change. White lines on the anisotropy heatmap indicate maximal growth orientations where anisotropy > 2. (E) Two-dimensional alignment of areal contribution of 2 DAI cells to 5 DAI leaves, compared with Col-0 leaf1, leaf8, and *pSPL9::SPL9r:Venus* (*SPL9r*) leaf1 by two-way ANOVA.

n = 3 (A and B) and 2 (D and E), n > 10 (C). Scale bars: 100 μm (A and D) and 10 μm (C).

See also Figure S4 and Video S2.

coupled with slower growth, likely contributes to the development of serrations in adult but not juvenile growth patterns (Figures 1B, S2G, and S4G) by enhancing the competence of the leaf margin to form these outgrowths[33,48]—a possibility that will be interesting to investigate further using both time-lapse imaging and more specific shape quantitation methods, given that our morphometric analyses above (Figures 2A, S2D, and S4E) do not capture age-dependent variation in leaf serration.

Prior work has shown that endoreduplication antagonizes cell proliferation and accompanies and contributes to cell expansion and differentiation in *A. thaliana* leaf development.[51] Therefore, we tested whether SPL9 acts to prevent endoreduplication. We found that the endoreduplication index (EI)[52] in Col-0 leaf1 is about twice as high as in leaf8 and is dramatically reduced by *pSPL9::SPL9r:Venus* (Figures 5A, S5A, and S5A′). By contrast, it is significantly increased in *spl9spl15* leaf8 (Figures 5A, S5A, and S5A′). To test whether this effect is sufficient to alter morphogenesis, we expressed *SPL9r* under the promoter of *LMI1*, which inhibits stipule growth (stipules are vestigial outgrowths at the flanks of young leaf primordia) by promoting endoreduplication.[53] We observed that stipule development was de-repressed in *pLMI1::SPL9r:*

Venus adult leaves (Figures 5B and 5B′), producing ectopic lobes as observed in *lmi1* mutants[53] (Figure S5B). Thus, in *pLMI1::SPL9r:Venus* leaves, SPL9 prevents endoreduplication (Figure 5C) in a manner that is sufficient to counteract stipule growth arrest. To test whether SPL9 is sufficient to prolong cell proliferation in a differentiated leaf cell type, we used guard cells because these represent the developmental endpoint of a well-characterized and limited cell division sequence that is pivotal for leaf physiology.[54,55] We found that *SPL9* expression under the *FAMA* promoter[56,57] triggered guard cell over-proliferation (Figures 5D and S5C), strongly indicating that *SPL9* is sufficient to maintain cell proliferation in diverse cellular contexts. Altogether, our results suggest that SPL9 sustains cell proliferation by preventing endocycle entry, hence retarding the transition from proliferation to differentiation and prolonging leaf morphogenesis.

Transcriptome signatures underlying SPL9-dependent retardation of the proliferation-to-differentiation transition

To understand how SPL9, as a transcription factor, coordinates cell proliferation and differentiation in leaf development, we examined the transcriptomes of developing leaves upon
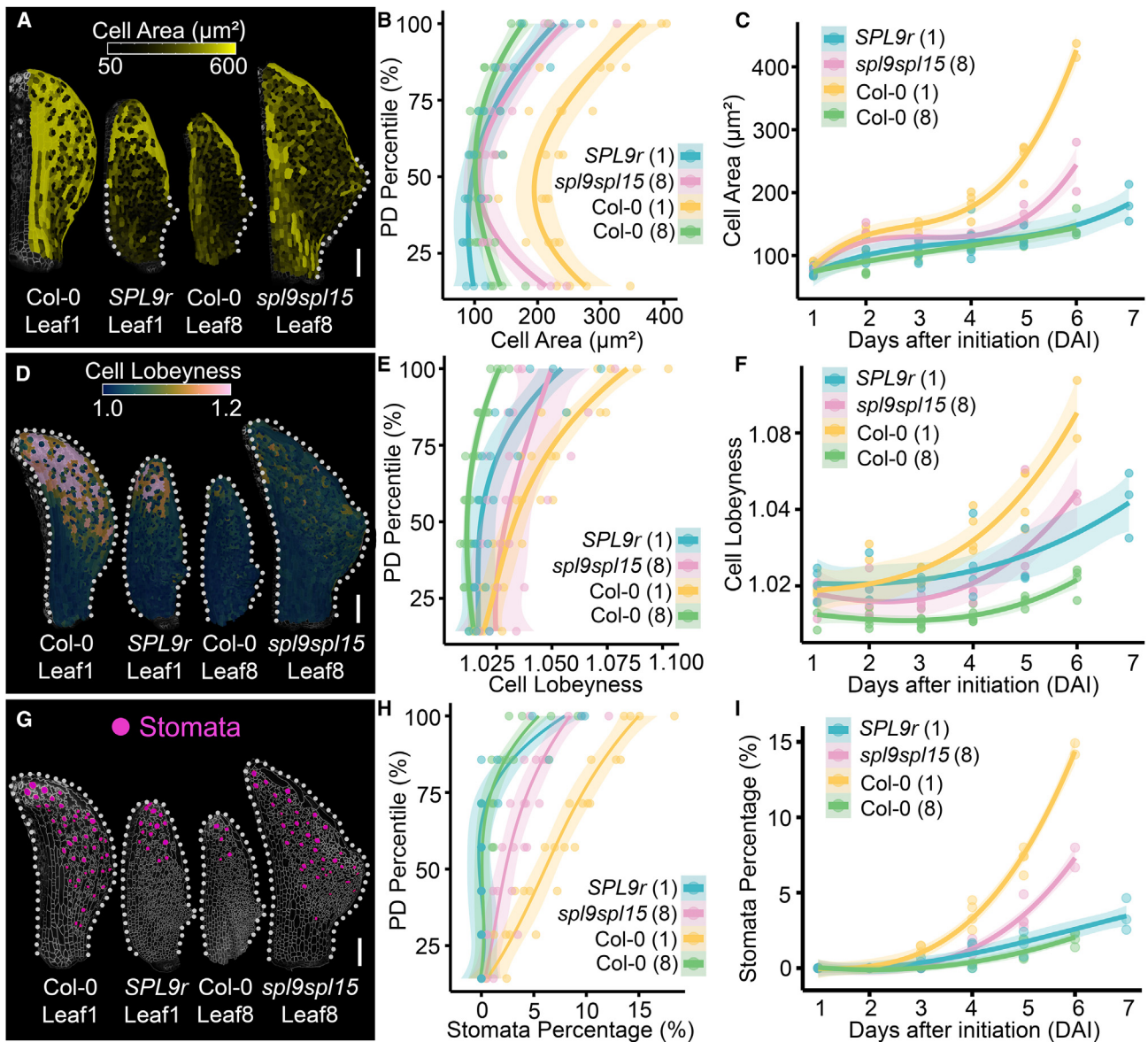
Figure 4. SPL9 retards cell differentiation

(A–I) Cell area (A–C), lobeyness (D–F), and stomatal emergence (G–I) were monitored during leaf early development. Measures at 5 DAI are visualized (representative heatmaps, A, D, and G) and plotted as a function of the distance from the leaf base (B, E, and H). Scale bars, 100 μm. Leaf-wide quantifications are tracked over time (C, F, and I). Cubic regression with 95% confidence interval (shaded). n = 3–4. *SPL9r*, *pSPL9::SPL9r:Venus*; numbers in brackets, leaf nodes.

SPL9 loss- and gain-of-function (*spl9*, *pSPL9::SPL9r:Venus*/*spl9spl15*) and inducible activation (dexamethasone [DEX]-induced *pSPL9::SPL9r:GR*). We found that cell proliferation transcription, as estimated by a digital mitotic index (DMI),[36] was promoted by SPL9—the DMI was reduced in *spl9* and increased in *pSPL9::SPL9r:Venus*/*spl9spl15* compared with wild type (Figure 5E) and rose upon SPL9 induction (Figure S5D). Consistent with this idea, transcriptome-wide gene set enrichment analyses (GSEAs)[58] showed that cell-cycle-related processes were overrepresented in *pSPL9::SPL9r: Venus*/*spl9spl15* or *SPL9*-induced transcriptomes, whereas they were underrepresented in *spl9* transcriptomes (Figures 5F, S5E, and S5E').

Unbiased transcriptome feature exploration by sparse partial least squares discriminant analysis (sPLS-DA)[59] indicated that SPL9 modifies the global transcriptome such that it moves forward in a notional age-dependent leaf organogenesis progression (calibration sequence: 5 mm leaf2, 5, 7, 9, and apex; Figures 5G and S5F), and backward along a leaf differentiation or maturation progression (leaf5 at 1 mm, 5 mm, 2 cm, and mature stages; Figures S5G and S5G'). These findings are congruent with our above growth analyses and suggest that SPL9 orchestrates leaf-wide transcriptional coordination of cell proliferation versus differentiation in favor of the former.

To search for specific gene expression programs that may underpin SPL9 action in growth modulation, we identified
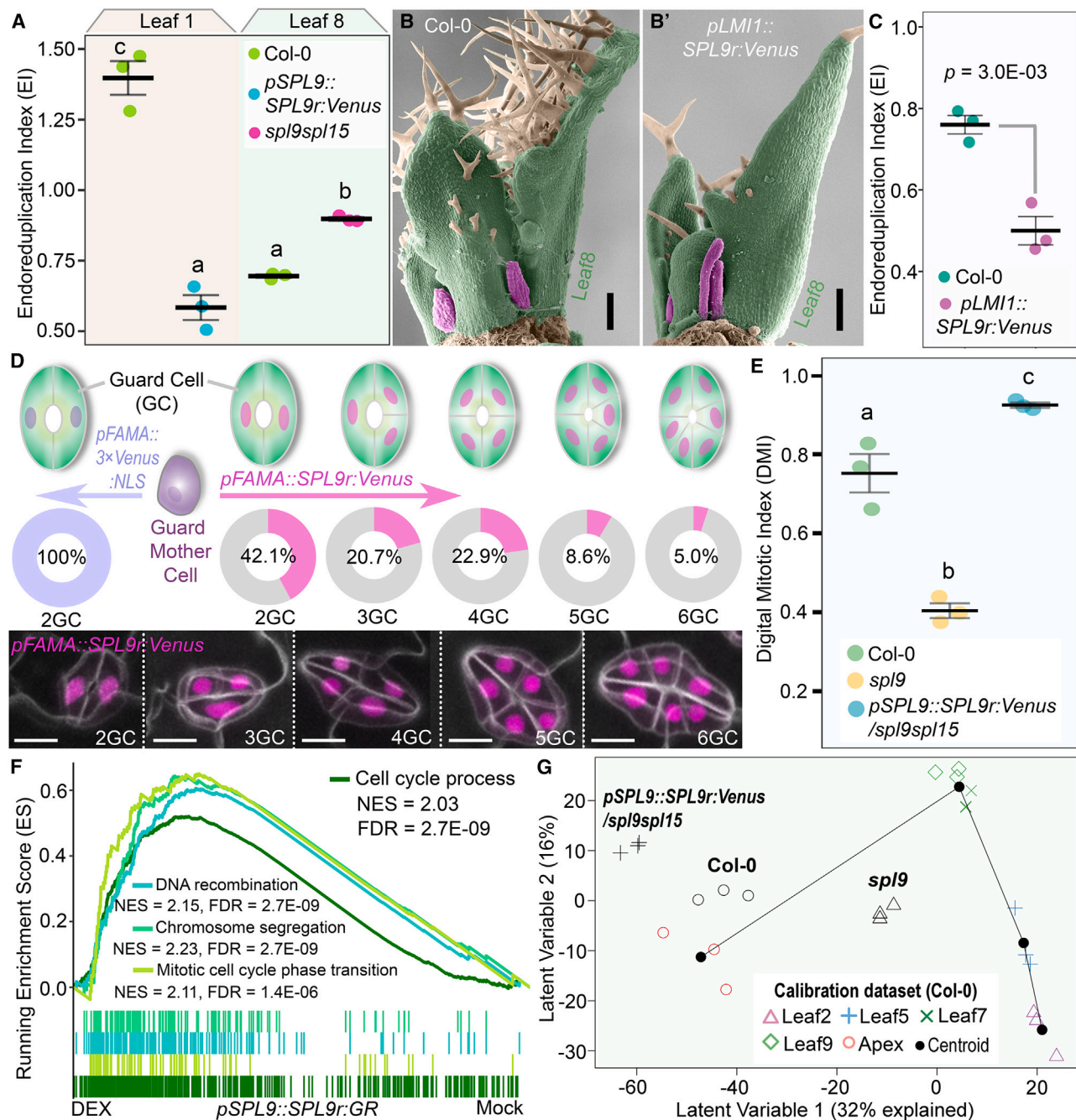
Figure 5. SPL9 sustains cell proliferation competence

(A) Endoreduplication index of indicated leaves. Mean ± SE. n = 3. a, b, and c, ANOVA-Tukey honestly significant difference (HSD).

(B and C) *pLMI1::SPL9r:Venus* fosters stipule (magenta) development while reducing leaf endoreduplication. Scale bar, 100 μm. Mean ± SE. p, Student's t test. n = 10 (B and B') and 3 (C).

(D) SPL9-driven guard cell over-proliferation. Top, stomata frequencies in a representative *pFAMA::SPL9r:Venus* line (n = 140) and the *pFAMA::3×Venus:NLS* (n > 500) control line (see Figure S5C); bottom, representative stomata in *pFAMA::SPL9r:Venus* leaves (scale bars, 10 μm).

(E–G) Transcriptome-based analyses of SPL9 effects on the cell proliferation-differentiation transition. n = 3. (E) Digital mitotic index. Mean ± SE; lowercase letters, ANOVA-Tukey HSD. (F) GSEA shows positive enrichment of cell-cycle-related processes upon SPL9 induction. NES, normalized enrichment score. (G) Developmental classification of transcriptomes by sPLS-DA. *SPL9*-dysregulated versus Col-0 transcriptomes (developing leaf primordia with shoot apex) were projected on a pseudo-developmental trajectory constructed with age-dependent leaf transcriptomes.

See also Figure S5.

SPL9-activated and -repressed gene sets as genes with reciprocal responses to *SPL9* loss- and gain-of-function (Figure S5H). We then confirmed that the SPL9-activated gene set responded to DEX induction in *pSPL9::SPL9r:GR* (Figure S5I) and mirrored *SPL9* time-dependent expression with a progressive accumulation in increasing leaf nodes and a decline during leaf maturation (Figures S5J and S5J′); the SPL9-repressed gene set showed the opposite trend (Figures S5I′, S5J, and S5J′). Gene Ontology (GO)[60,61] analysis of these respective gene sets indicated that, contrary to SPL9-repressed genes, SPL9-activated genes were heavily enriched in cell-cycle-related terms, whereas they were underrepresented in processes of photosynthetic machinery differentiation (Figure S5K), which is thought to associate with the cell proliferation-to-expansion transition during leaf development.[37] Thus, time-dependent expression of *SPL9* results in the activation of cell-cycle-related gene expression and the repression of differentiation-associated transcription during leaf development.

SPL9 modulates cell cycle and growth by directly activating *CYCD3* genes

Among SPL9-activated cell-cycle-related genes, all three members of the D3-type cyclin gene family showed SPL9-dependent expression in our transcriptomes (Figures S6A and S6A′). In view of their critical roles in cell cycle maintenance,[62–64] which we have identified as an important component of SPL9 function, we considered whether CYCD3s might mediate SPL9 action in heteroblasty. We tested this idea using genetic analyses and found that *cycd3;1-3* and *spl9cycd3;1-3* phenocopied *spl9* leaf heteroblasty defects, such as a delayed transition from a round to an oval shape (Figures 6A and 6A′), indicating that *SPL9* and *CYCD3s* act in the same genetic pathway. Combined, these data suggest that *CYCD3* genes may function downstream of SPL9 in heteroblasty.

Three lines of evidence indicate that *CYCD3* genes are direct transcriptional targets of SPL9. First, we validated that SPL9 is necessary and sufficient for *CYCD3* expression by qPCR (Figures 6B and S6B). Second, chromatin immunoprecipitation (ChIP) showed that SPL9 could associate with *CYCD3* promoters *in planta* via the enriched GTAC motif[65] that SPLs are predicted to bind (Figures 6C and S6C–S6E′). Third, a *CYCD3;3* transgene rescued the heteroblastic delay of *cycd3;1-3* but not *spl9* (Figures S6F and S6F′), and mutating the GTAC motifs in its promoter prevents complementation of *cycd3;1-3* (Figure S6F), both of which suggest the necessity of SPL9-GTAC binding for *CYCD3* action in leaf heteroblasty.

To test the precise functional relevance of *CYCD3* activation by SPL9 for leaf morphology, we carried out a genetic bypass experiment where we expressed *CYCD3;2* and *CYCD3;3* in *spl9* under the joint control of the *SPL9* promoter and the miRNA156 target site. We found that both constructs rescued *spl9* heteroblasty defects (Figure 6D), indicating that CYCD3s can bypass the requirement for SPL9 in heteroblasty. Consistent with this idea, expressing *CYCD3;1* in the *LMI1* domain causes stipules to develop into ectopic lobes at leaf bases (Figure S6G), mirroring the *SPL9* effect we described previously (Figure S5B). Similarly, *pFAMA::CYCD3;2* was previously reported to cause supernumerary divisions in guard cells,[66] and we show here the same effect for *pFAMA::SPL9r:Venus* (Figure 5D).

Altogether, these findings indicate that *CYCD3* genes likely act as major molecular mediators of SPL9 function in heteroblasty by preventing entry into endoreduplication, thus prolonging the duration of cell proliferation.

Our hypothesis that *CYCD3* genes are major mediators of SPL9 function in growth reprogramming is supported by organ shape analysis and genetics. However, because SPL9 regulates hundreds of genes, and there are feedbacks between the cell cycle and organ growth control,[32,67] it is in principle possible that CYCD3 and SPL9 have non-overlapping effects at the cellular level that then converge to comparable tissue-level phenotypes. To evaluate whether CYCD3s and SPL9 have equivalent effects at the cellular scale, which should be the case if *CYCD3* genes are major determinants of SPL9 function across biological scales, we studied cellular growth in *cycd3;1-3* leaf8 using time-lapse imaging. Four lines of evidence support the congruence of SPL9 and CYCD3 functions in programming cellular growth in the leaf. First, we observed a rapid decline in proliferation accompanied by a reduction in growth rate, in *cycd3;1-3* leaf8 (Figures 6E, 6F, 6I, S6H, S6N1, and S6N2; Video S3), reminiscent of the fast release of proliferative growth seen in the absence of *SPL9* (Col-0 leaf1 and *spl9spl15* leaf8, Figures 1E, 1H, 2B, and 2C), although this effect started earlier in *cycd3;1-3*. Second, we found higher anisotropic growth (PD/ML growth ratio, Figures S6I and S6N3), accelerated cell expansion (Figures 6G, 6I, S6J, and S6N4), and precocious differentiation (Figures 6H, S6K, and S6N5) in *cycd3;1-3* versus Col-0, resembling that of the *spl9spl15* mutant (Figures S6H–S6K). Third, fate maps in *cycd3;1-3* leaf8 showed a basipetal shift in the contributions of growth to leaf histogenesis (Figures 6J, S6L, and S6L′), similar to that observed in *spl9spl15* (Figures S2U, S6L, and S6L′), indicating the juvenilization of leaf8 cellular development in *cycd3;1-3* plants. Finally, *cycd3;1-3* cells showed a significant enlargement before undergoing the fast growth and proliferation release (Figures S6M and S6M′), mirroring the cell behavior that precedes the proliferation burst in the absence of *SPL9* (Figure 2H). These findings indicate that CYCD3 proteins, similar to SPL9, regulate growth in conjunction with coordinating cell size and division competence. As such, these results show that SPL9 times the cell cycle by transcriptionally regulating *CYCD3* genes and that this effect is crucial for the heteroblastic reprogramming of cellular growth patterns.

In summary, our findings suggest a cellular growth model for leaf heteroblasty (Figure 7) in which an age-dependent, SPL9 PD gradient, regulates leaf cellular growth and coordinates proliferation and differentiation (Figure 7A) via directly regulating *CYCD3* genes and preventing cell cycle exit and the transition to endocycling (Figure 7B).

DISCUSSION

We have investigated the time-dependent regulation of growth that underpins leaf heteroblasty. We demonstrated how SPL9 reprograms cellular growth to cause age-dependent changes in leaf form. Among several tightly connected growth features, namely, growth amount (area extension), direction (anisotropy, PD versus ML growth), rate, and duration, we identified sustained proliferative growth as the key mechanism underlying
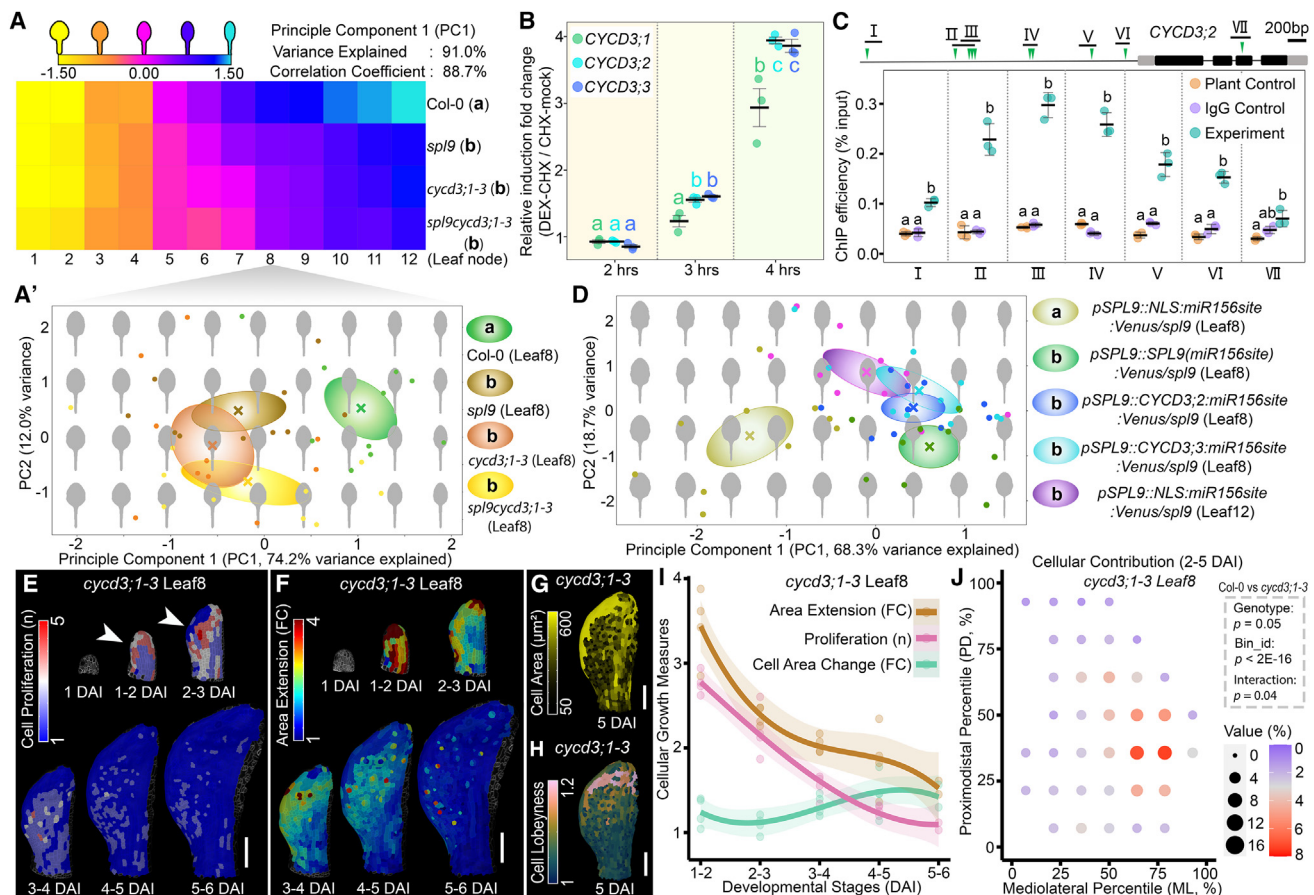
Figure 6. CYCD3 genes bypass the requirement for SPL9 in heteroblasty

(A and A′) Genetic interaction between *spl9* and *cycd3;1-3*. Heatmap of mean PC1 (A, heteroblasty index, see Figure 2A) from leaf morphometric PCA analysis. Leaf8 results, presented in shape-space (A′). Cross, mean; ellipse, SE. (a and b), ANCOVA-Tukey HSD (A) or ANOVA-Tukey HSD of PC1 (A′).

(B) SPL9 induces *CYCD3* expression. *pSPL9::SPL9r:GR* seedlings were treated with cycloheximide (CHX)-mock or dexamethasone (DEX)-CHX for indicated periods. *CYCD3* induction was examined by RT-qPCR. Mean ± SE. Lowercase letters in the same color, Tukey HSD, for the indicated gene.

(C) SPL9 can associate with the *CYCD3;2* upstream region *in planta*. Top, gene model with ChIP-targets numbered. Line, regulatory sequence (promoter and intron); blocks, exons (light gray, untranslated region [UTR]; black, coding sequence [CDS]); green triangles, GTAC boxes.[65] The experiment group (*pSPL9::SPL9r:Venus/spl9spl15* treated with anti-GFP) was compared with two controls: antibody control, *pSPL9::SPL9r:Venus/spl9spl15* with immunoglobulin G (IgG); plant control, *pSPL9::NLS:miR156r:Venus* with anti-GFP. Mean ± SE. Compact letters, ANOVA-Tukey HSD for each block.

(D) *CYCD3* genes bypass *SPL9* loss-of-function in leaf heteroblasty. PCA-based shape-space plot of leaf8s and leaf12 control. (a and b), ANOVA-Tukey HSD test of PC1. Cross, mean; ellipse, SE.

(E–H) Representative heatmaps of cell proliferation (E), area extension (F), cell area (G), and lobeyness (H) for *cycd3;1-3* leaf8. Arrowheads, accelerated proliferation burst. DAI, days after initiation. Scale bars, 100 μm.

(I) Growth dynamics of *cycd3;1-3* leaf8. Cubic regression with 95% confidence interval.

(J) 2D (PD/ML) alignment of cellular contribution (2–5 DAI) in *cycd3;1-3* leaf8. Two-way ANOVA, compared with Col-0 leaf8 (Figure 1P).

n = 10 (A, A′, and D), 3 (B and C), and 3–4 (E–J).

See also Figure S6 and Video S3.

developmental reprogramming controlled by SPL9. Specifically, SPL9 protracts cell cycle length at the individual cell level and prolongs the duration of proliferative growth at the cell population level by blocking the mitotic cycle-endocycle transition. In this way, SPL9 antagonizes a proliferation burst that is repressed as the plant ages to yield the adult leaf shape. In the absence of SPL9 repression, this burst reappears and restores leaf growth to a juvenile pattern. As juvenile leaves, which do not express *SPL9*, develop before adult ones, the proliferation burst can be considered a default state for the leaf development program in this species. We identified three cyclin genes, *CYCD3;1-3*, as a

central point connecting the SPL9 transcription factor to cell cycle timing and growth reprogramming. Although SPL9 regulates a complex gene network that is involved in many aspects of plant aging,[12,14,16,19,21–24] *CYCD3* genes are sufficient to bypass the requirement for *SPL9* in heteroblasty when expressed in the *SPL9* domain. In this way, SPL9, through transcriptional activation of *CYCD3*, links the unfolding of developmental time across three temporal scales: the cell cycle, the timing of the PD development of an organ, and the age of the whole organism. Notably, it was recently shown that an *SPL* gene distantly related to *SPL9* is required for meristem dormancy in the liverwort *Marchantia*
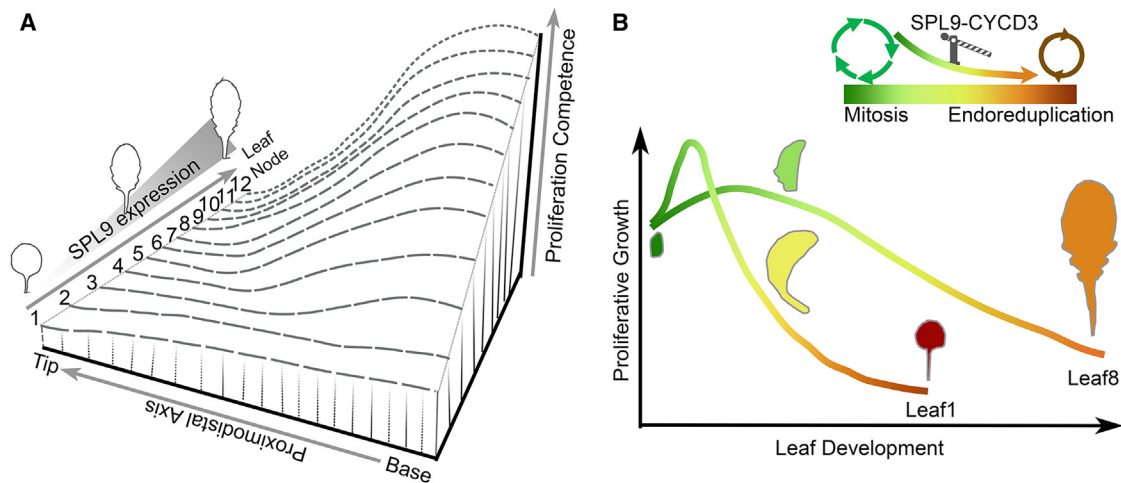
Figure 7. Age-dependent cell cycle timing contributes to heteroblastic leaf development

(A) Landscape model showing how SPL9 modulates cell proliferation in developing leaf primordia. Upon shoot age-dependent *SPL9* accumulation (front-to-back), cell proliferation competence increases (ordinate), resulting in a protracted proliferation period (at the tissue level) that is associated with prolonged cell cycle length (at the cellular level). This inter-leaf divergence is accompanied by intra-leaf changes along the proximodistal axis (right-to-left), reflecting *SPL9* basipetal decline during leaf maturation.

(B) Schematic showing how sustained cell proliferation enables leaf heteroblasty. An early stage "proliferation burst" distinguishes the leaf1 growth pattern from that of leaf8, where the SPL9-CYCD3 module prevents exit from the cell cycle and limits the rate but prolongs the duration of proliferative growth. Color gradient reflects changes in average endoreduplication level in developing leaves.

polymorpha.[68] In this context, it will be interesting to investigate whether this function involves regulation of the cell cycle as we describe here for *A. thaliana*. This could help clarify if the function of SPLs in modulating proliferative growth was ancestral in land plants, and then became part of the vegetative change program in seed plants.

Our findings also help clarify the complex interrelationships between cell division and growth. There is a longstanding debate on whether growth drives cell proliferation or vice versa, although, in some contexts, they have been shown to be separable.[69–72] Recent evidence has suggested a dual control of growth and cell division patterns by hypothetical upstream regulators in leaf development.[32] Our data indicate the SPL9-CYCD3 module fulfills such a role and is a key control point in leaf development, because SPL9 provides spatiotemporally encoded information that regulates growth, in association with its direct input into the cell cycle. Because plant growth depends on the cell wall yielding to turgor pressure, there are various possibilities to account for why lower SPL9-CYCD3 levels lead to faster growth (Figures S1L2, S2N2, and S6N2). First, SPL9 may ultimately affect cell wall properties concurrently with regulating *CYCD3*, an idea supported by the finding that cell growth-related gene expression, including expansin gene transcription,[73–76] is modulated by SPL9 in our transcriptome data (Figures S7A–S7C). More strikingly, we observed that SPL9 functions to increase the thickness of the outer epidermal wall during the proliferation burst period (Figures S7D–S7G). Second, there may be feedback or regulatory linkages between cell division status and wall extensibility that function to coordinate cell proliferation and growth; a related possibility is that CYCD3 participates in transcriptional complexes that affect growth and differentiation independently of the cell cycle.[77] Additionally, from a

biophysical perspective, larger cells that form primordia with reduced *SPL9/CYCD3* expression (Figures 2H and S6M′) will accumulate higher stress in their surface walls[78] and would also have higher strain.[42] Thus, in a strain-based growth model, they would be expected to grow faster (Figures S7H–S7K). In this context, the coexistence of fast growth and the proliferation burst in such cells is noteworthy, because mechanical simulations indicate that a reduction in cell size (which is a consequence of cell division) would tend to slow down growth (Figures S7H–S7K), all else being equal. This observation suggests that growth-promoting mechanisms active in the "proliferation burst" population can override this potentially inhibitory effect. Thus, a fundamental future challenge will be to understand how biological regulation interacts with constraints laid down by cell and tissue mechanics to generate plant form and its diversity.

An important aspect of the SPL9-mediated growth control we describe here is that its heterogeneous expression in different leaf nodes modulates developmental scaling in organ morphogenesis, resulting in differences in leaf shape in different nodes. This is different to cases of organogenesis where scaling ensures uniformity of organ shape independent of size variance; for example, in the development of the *Drosophila* wing, which, similar to a plant leaf, is a laminar organ.[79] In contrast to this, unfolding of the SPL9/CYCD3-dependent temporal program leads to predictable leaf shape heterogeneity with plant aging. This regulation reflects the distinctive coupling of plant growth and the cell cycle via the SPL9-CYCD3 module. Notably, unlike the findings we report here for SPL9-CYCD3, not all cell cycle perturbations are associated with plant organ shape or size changes.[2,24,70,71,80–84] This indicates that, although control of cell proliferation and organ geometry can be uncoupled, the links between them are an important part of plant development.

The function of the SPL9-CYCD3 module in leaf heteroblastic growth also has implications for the integration of metabolic and physiological signals with the cell cycle and organ morphogenesis. For example, both *SPL9* and *CYCD3* expression respond to sugar levels,[85–88] while leaf heteroblasty may influence plant photosynthetic capacity.[89,90] This indicates a positive feedback loop between the SPL9-CYCD3 module and photosynthate (sugar) accumulation, which resonates with the original conception of leaf heteroblasty as photosynthate-nurtured development.[7] In the future, it will be important to understand the nexus of SPL9 and photosynthetic physiology and to explore the potential modulation of the processes characterized here for plant adaptation in changing environments and for the improvement of plant performance.

STAR★METHODS

Detailed methods are provided in the online version of this paper and include the following:

- KEY RESOURCES TABLE
- RESOURCE AVAILABILITY
  - Lead contact
  - Materials availability
  - Data and code availability
- EXPERIMENTAL MODEL AND SUBJECT DETAILS
  - Bacteria and cultivation
  - Plants and growth conditions
- METHOD DETAILS
  - Plasmid construction and genetic materials
  - Microscopy and image analysis
  - Cellular growth quantification
  - Growth animation
  - Growth alignment
  - Expression analysis
  - Mature leaf quantification
  - Ploidy analysis
  - Transcriptome analysis
  - ChIP experiment
  - FEM modelling
- QUANTIFICATION AND STATISTICAL ANALYSES

AUTHOR CONTRIBUTIONS

X.-M.L., H.J., and M.T. designed the experiments. X.-M.L. conducted the majority of the work, including experiments, data analyses, and validation. H.J. generated genetic materials and performed most of the time-lapse imaging, and S.S. was instrumental in MGX analyses and associated methods (e.g., 2D growth alignment). C.B., P.N., and S.L. were involved in RNA-seq and relevant analyses, and G.M. did computational simulations with S.S.'s help. R.L., D.K., and P.H. took part in microscopy and related data processing, and A.R. contributed to data quantification and interpretation. U.N. performed the TEM assay, and R.S.S. contributed to method development. X.-M.L. prepared figures and the draft, and X.-M.L. and M.T. wrote the manuscript with input from other authors (particularly S.S.). M.T. supervised this study.

REFERENCES

1. Collinet, C., and Lecuit, T. (2021). Programmed and self-organized flow of information during morphogenesis. Nat. Rev. Mol. Cell Biol. *22*, 245–265.

2. Hong, L., DuMond, M., Zhu, M., Tsugawa, S., Li, C.B., Boudaoud, A., Hamant, O., and Roeder, A.H.K. (2018). Heterogeneity and robustness in plant morphogenesis: from cells to organs. Annu. Rev. Plant Biol. *69*, 469–495.

3. Ebisuya, M., and Briscoe, J. (2018). What does time mean in development? Development *145*, dev164368.

4. Rayon, T., Stamataki, D., Perez-Carrasco, R., Garcia-Perez, L., Barrington, C., Melchionda, M., Exelby, K., Lazaro, J., Tybulewicz, V.L.J., Fisher, E.M.C., et al. (2020). Species-specific pace of development is associated with differences in protein stability. Science *369*, eaba7667.

5. Matsuda, M., Hayashi, H., Garcia-Ojalvo, J., Yoshioka-Kobayashi, K., Kageyama, R., Yamanaka, Y., Ikeya, M., Toguchida, J., Alev, C., and Ebisuya, M. (2020). Species-specific segmentation clock periods are due to differential biochemical reaction speeds. Science *369*, 1450–1455.

6. Ashby, E. (1948). Studies in the morphogenesis of leaves. I. An essay on leaf shape. New Phytol. *47*, 153–176.

7. Goebel, K. (1908). Einleitung in die Experimentelle Morphologie der Pflanzen (BG Teubner).

8. Poethig, R.S. (1990). Phase-change and the regulation of shoot morphogenesis in plants. Science *250*, 923–930.

9. Ambros, V. (2011). MicroRNAs and developmental timing. Curr. Opin. Genet. Dev. *21*, 511–517.

10. Poethig, R.S. (2009). Small RNAs and developmental timing in plants. Curr. Opin. Genet. Dev. *19*, 374–378.

11. Xing, S., Salinas, M., Höhmann, S., Berndtgen, R., and Huijser, P. (2010). miR156-targeted and nontargeted SBP-box transcription factors act in concert to secure male fertility in *Arabidopsis*. Plant Cell *22*, 3935–3950.

12. Xu, M., Hu, T., Zhao, J., Park, M.Y., Earley, K.W., Wu, G., Yang, L., and Poethig, R.S. (2016). Developmental functions of miR156-regulated *squamosa PROMOTER BINDING PROTEIN-LIKE* (*SPL*) genes in *Arabidopsis thaliana*. PLoS Genet. *12*, e1006263.

13. He, J., Xu, M., Willmann, M.R., McCormick, K., Hu, T., Yang, L., Starker, C.G., Voytas, D.F., Meyers, B.C., and Poethig, R.S. (2018). Threshold-dependent repression of *SPL* gene expression by miR156/miR157 controls vegetative phase change in *Arabidopsis thaliana*. PLoS Genet. *14*, e1007337.

14. Wang, J.W., Czech, B., and Weigel, D. (2009). miR156-regulated SPL transcription factors define an endogenous flowering pathway in *Arabidopsis thaliana*. Cell *138*, 738–749.

15. Fouracre, J.P., and Poethig, R.S. (2019). Role for the shoot apical meristem in the specification of juvenile leaf identity in *Arabidopsis*. Proc. Natl. Acad. Sci. USA *116*, 10168–10177.

16. Wu, G., Park, M.Y., Conway, S.R., Wang, J.W., Weigel, D., and Poethig, R.S. (2009). The sequential action of miR156 and miR172 regulates developmental timing in *Arabidopsis*. Cell *138*, 750–759.

17. Zhao, J., Doody, E., and Poethig, R.S. (2023). Reproductive competence is regulated independently of vegetative phase change in *Arabidopsis thaliana*. Curr. Biol. *33*, 487–497.e2.

18. Schwarz, S., Grande, A.V., Bujdoso, N., Saedler, H., and Huijser, P. (2008). The microRNA regulated SBP-box genes *SPL9* and *SPL15* control shoot maturation in Arabidopsis. Plant Mol. Biol. *67*, 183–195.

19. Wang, J.W., Schwab, R., Czech, B., Mica, E., and Weigel, D. (2008). Dual effects of miR156-targeted *SPL* genes and *CYP78A5/KLUH* on plastochron length and organ size in *Arabidopsis thaliana*. Plant Cell *20*, 1231–1243.

20. Hyun, Y., Richter, R., Vincent, C., Martinez-Gallegos, R., Porri, A., and Coupland, G. (2016). Multi-layered regulation of SPL15 and cooperation with SOC1 integrate endogenous flowering pathways at the *Arabidopsis* shoot meristem. Dev. Cell *37*, 254–266.

21. Hu, T., Manuela, D., and Xu, M. (2023). Squamosa PROMOTER BINDING PROTEIN-LIKE 9 and 13 repress *BLADE-ON-PETIOLE 1* and *2* directly to promote adult leaf morphology in Arabidopsis. J. Exp. Bot. *74*, 1926–1939.

22. Tao, X.Y., Guan, X.Y., Hong, G.J., He, Y.Q., Li, S.J., Feng, S.L., Wang, J., Chen, G., Xu, F., Wang, J.W., et al. (2023). Biotinylated Tn5 transposase-mediated CUT&Tag efficiently profiles transcription factor-DNA interactions in plants. Plant Biotechnol. J. *21*, 1191–1205.

23. Wang, J.-W. (2016). The multifaceted roles of miR156-targeted SPL transcription factors in plant developmental transitions. In Plant Transcription Factors (Academic Press), pp. 281–293.

24. Tang, H.B., Wang, J., Wang, L., Shang, G.D., Xu, Z.G., Mai, Y.X., Liu, Y.T., Zhang, T.Q., and Wang, J.W. (2023). Anisotropic cell growth at the leaf base promotes age-related changes in leaf shape in *Arabidopsis thaliana*. Plant Cell *35*, 1386–1407.

25. Gou, J.Y., Felippes, F.F., Liu, C.J., Weigel, D., and Wang, J.W. (2011). Negative regulation of anthocyanin biosynthesis in *Arabidopsis* by a miR156-targeted SPL transcription factor. Plant Cell *23*, 1512–1522.

26. Yu, N., Cai, W.J., Wang, S., Shan, C.M., Wang, L.J., and Chen, X.Y. (2010). Temporal control of trichome distribution by MicroRNA156-targeted *SPL* genes in *Arabidopsis thaliana*. Plant Cell *22*, 2322–2335.

27. Zhang, T.Q., Lian, H., Tang, H., Dolezal, K., Zhou, C.M., Yu, S., Chen, J.H., Chen, Q., Liu, H., Ljung, K., et al. (2015). An intrinsic microRNA timer regulates progressive decline in shoot regenerative capacity in plants. Plant Cell *27*, 349–360.

28. Rubio-Somoza, I., Zhou, C.M., Confraria, A., Martinho, C., von Born, P., Baena-Gonzalez, E., Wang, J.W., and Weigel, D. (2014). Temporal control of leaf complexity by miRNA-regulated licensing of protein complexes. Curr. Biol. *24*, 2714–2719.

29. Bhatia, N., Runions, A., and Tsiantis, M. (2021). Leaf shape diversity: from genetic modules to computational models. Annu. Rev. Plant Biol. *72*, 325–356.

30. Maugarny-Calès, A., and Laufs, P. (2018). Getting leaves into shape: a molecular, cellular, environmental and evolutionary view. Development *145*, dev161646.

31. Satterlee, J.W., and Scanlon, M.J. (2019). Coordination of leaf development across developmental axes. Plants (Basel) *8*, 433.

32. Fox, S., Southam, P., Pantin, F., Kennaway, R., Robinson, S., Castorina, G., Sánchez-Corrales, Y.E., Sablowski, R., Chan, J., Grieneisen, V., et al. (2018). Spatiotemporal coordination of cell division and growth during organ morphogenesis. PLoS Biol. *16*, e2005952.

33. Kierzkowski, D., Runions, A., Vuolo, F., Strauss, S., Lymbouridou, R., Routier-Kierzkowska, A.L., Wilson-Sánchez, D., Jenke, H., Galinha, C., Mosca, G., et al. (2019). A growth-based framework for leaf shape development and diversity. Cell *177*, 1405–1418.e17.

34. Kuchen, E.E., Fox, S., de Reuille, P.B., Kennaway, R., Bensmihen, S., Avondo, J., Calder, G.M., Southam, P., Robinson, S., Bangham, A., et al. (2012). Generation of leaf shape through early patterns of growth and tissue polarity. Science *335*, 1092–1096.

35. Donnelly, P.M., Bonetta, D., Tsukaya, H., Dengler, R.E., and Dengler, N.G. (1999). Cell cycling and cell enlargement in developing leaves of *Arabidopsis*. Dev. Biol. *215*, 407–419.

36. Efroni, I., Blum, E., Goldshmidt, A., and Eshed, Y. (2008). A protracted and dynamic maturation schedule underlies *Arabidopsis* leaf development. Plant Cell *20*, 2293–2306.

37. Andriankaja, M., Dhondt, S., De Bodt, S., Vanhaeren, H., Coppens, F., De Milde, L., Mühlenbock, P., Skirycz, A., Gonzalez, N., Beemster, G.T., et al. (2012). Exit from proliferation during leaf development in *Arabidopsis thaliana*: a not-so-gradual process. Dev. Cell *22*, 64–78.

38. Rodriguez, R.E., Schommer, C., and Palatnik, J.F. (2016). Control of cell proliferation by microRNAs in plants. Curr. Opin. Plant Biol. *34*, 68–76.

39. Sarvepalli, K., Das Gupta, M., Challa, K.R., and Nath, U. (2019). Molecular cartography of leaf development - role of transcription factors. Curr. Opin. Plant Biol. *47*, 22–31.

40. Coen, E., Kennaway, R., and Whitewoods, C. (2017). On genes and form. Development *144*, 4203–4213.

41. Elsner, J., Michalski, M., and Kwiatkowska, D. (2012). Spatiotemporal variation of leaf epidermal cell growth: a quantitative analysis of *Arabidopsis thaliana* wild-type and triple *cyclinD3* mutant plants. Ann. Bot. *109*, 897–910.

42. Sapala, A., Runions, A., Routier-Kierzkowska, A.L., Das Gupta, M., Hong, L., Hofhuis, H., Verger, S., Mosca, G., Li, C.B., Hay, A., et al. (2018). Why plants make puzzle cells, and how their shape emerges. eLife *7*, e32794.

43. Ichihashi, Y., Kawade, K., Usami, T., Horiguchi, G., Takahashi, T., and Tsukaya, H. (2011). Key proliferative activity in the junction between the leaf blade and leaf petiole of Arabidopsis. Plant Physiol. *157*, 1151–1162.

44. Le Gloanec, C., Collet, L., Silveira, S.R., Wang, B., Routier-Kierzkowska, A.L., and Kierzkowski, D. (2022). Cell type-specific dynamics underlie cellular growth variability in plants. Development *149*, dev200783.

45. Zhang, Z., Runions, A., Mentink, R.A., Kierzkowski, D., Karady, M., Hashemi, B., Huijser, P., Strauss, S., Gan, X., Ljung, K., et al. (2020). A WOX/auxin biosynthesis module controls growth to shape leaf form. Curr. Biol. *30*, 4857–4868.e6.

46. D'Ario, M., and Sablowski, R. (2019). Cell size control in plants. Annu. Rev. Genet. *53*, 45–65.

47. Pujari, I., Thomas, A., Rai, P.S., Satyamoorthy, K., and Babu, V.S. (2021). Cell size: a key determinant of meristematic potential in plant protoplasts. aBIOTECH *2*, 96–104.

48. Bilsborough, G.D., Runions, A., Barkoulas, M., Jenkins, H.W., Hasson, A., Galinha, C., Laufs, P., Hay, A., Prusinkiewicz, P., and Tsiantis, M. (2011). Model for the regulation of *Arabidopsis thaliana* leaf margin development. Proc. Natl. Acad. Sci. USA *108*, 3424–3429.

49. Savaldi-Goldstein, S., Peto, C., and Chory, J. (2007). The epidermis both drives and restricts plant shoot growth. Nature *446*, 199–202.

50. Lu, P., Porat, R., Nadeau, J.A., and O'Neill, S.D. (1996). Identification of a meristem L1 layer-specific gene in Arabidopsis that is expressed during embryonic pattern formation and defines a new class of homeobox genes. Plant Cell *8*, 2155–2168.

51. Lang, L., and Schnittger, A. (2020). Endoreplication - a means to an end in cell growth and stress response. Curr. Opin. Plant Biol. *54*, 85–92.

52. Barow, M., and Meister, A. (2003). Endopolyploidy in seed plants is differently correlated to systematics, organ, life strategy and genome size. Plant Cell & Environment *26*, 571–584.

53. Vuolo, F., Kierzkowski, D., Runions, A., Hajheidari, M., Mentink, R.A., Gupta, M.D., Zhang, Z., Vlad, D., Wang, Y., Pecinka, A., et al. (2018).

LMI1 homeodomain protein regulates organ proportions by spatial modulation of endoreduplication. Genes Dev. *32*, 1361–1366.

54. Lee, L.R., and Bergmann, D.C. (2019). The plant stomatal lineage at a glance. J. Cell Sci. *132*, jcs228551.

55. Pillitteri, L.J., and Torii, K.U. (2012). Mechanisms of stomatal development. Annu. Rev. Plant Biol. *63*, 591–614.

56. Ohashi-Ito, K., and Bergmann, D.C. (2006). *Arabidopsis* FAMA controls the final proliferation/differentiation switch during stomatal development. Plant Cell *18*, 2493–2505.

57. Pillitteri, L.J., Sloan, D.B., Bogenschutz, N.L., and Torii, K.U. (2007). Termination of asymmetric cell division and differentiation of stomata. Nature *445*, 501–505.

58. Subramanian, A., Tamayo, P., Mootha, V.K., Mukherjee, S., Ebert, B.L., Gillette, M.A., Paulovich, A., Pomeroy, S.L., Golub, T.R., Lander, E.S., et al. (2005). Gene set enrichment analysis: a knowledge-based approach for interpreting genome-wide expression profiles. Proc. Natl. Acad. Sci. USA *102*, 15545–15550.

59. Lê Cao, K.A.L., Boitard, S., and Besse, P. (2011). Sparse PLS discriminant analysis: biologically relevant feature selection and graphical displays for multiclass problems. BMC Bioinformatics *12*, 253.

60. Ashburner, M., Ball, C.A., Blake, J.A., Botstein, D., Butler, H., Cherry, J.M., Davis, A.P., Dolinski, K., Dwight, S.S., Eppig, J.T., et al. (2000). Gene Ontology: tool for the unification of biology. The Gene Ontology Consortium. Nat. Genet. *25*, 25–29.

61. Gene Ontology Consortium (2021). The Gene Ontology resource: enriching a gold mine. Nucleic Acids Res. *49*, D325–D334.

62. Dewitte, W., Riou-Khamlichi, C., Scofield, S., Healy, J.M., Jacqmard, A., Kilby, N.J., and Murray, J.A. (2003). Altered cell cycle distribution, hyperplasia, and inhibited differentiation in Arabidopsis caused by the D-type cyclin CYCD3. Plant Cell *15*, 79–92.

63. Dewitte, W., Scofield, S., Alcasabas, A.A., Maughan, S.C., Menges, M., Braun, N., Collins, C., Nieuwland, J., Prinsen, E., Sundaresan, V., et al. (2007). *Arabidopsis* CYCD3 D-type cyclins link cell proliferation and endocycles and are rate-limiting for cytokinin responses. Proc. Natl. Acad. Sci. USA *104*, 14537–14542.

64. Menges, M., Samland, A.K., Planchais, S., and Murray, J.A. (2006). The D-type cyclin CYCD3;1 is limiting for the G1-to-S-phase transition in *Arabidopsis*. Plant Cell *18*, 893–906.

65. Birkenbihl, R.P., Jach, G., Saedler, H., and Huijser, P. (2005). Functional dissection of the plant-specific SBP-domain: overlap of the DNA-binding and nuclear localization domains. J. Mol. Biol. *352*, 585–596.

66. Yang, K., Wang, H., Xue, S., Qu, X., Zou, J., and Le, J. (2014). Requirement for A-type cyclin-dependent kinase and cyclins for the terminal division in the stomatal lineage of *Arabidopsis*. J. Exp. Bot. *65*, 2449–2461.

67. Shimotohno, A., Aki, S.S., Takahashi, N., and Umeda, M. (2021). Regulation of the plant cell cycle in response to hormones and the environment. Annu. Rev. Plant Biol. *72*, 273–296.

68. Streubel, S., Deiber, S., Rötzer, J., Mosiolek, M., Jandrasits, K., and Dolan, L. (2023). Meristem dormancy in *Marchantia polymorpha* is regulated by a liverwort-specific miRNA and a clade III *SPL* gene. Curr. Biol. *33*, 660–674.e4.

69. Devany, J., Falk, M.J., Holt, L.J., Murugan, A., and Gardel, M.L. (2023). Epithelial tissue confinement inhibits cell growth and leads to volume-reducing divisions. Dev. Cell *58*, 1462–1476.e8.

70. Roeder, A.H., Chickarmane, V., Cunha, A., Obara, B., Manjunath, B.S., and Meyerowitz, E.M. (2010). Variability in the control of cell division underlies sepal epidermal patterning in *Arabidopsis thaliana*. PLoS Biol. *8*, e1000367.

71. Neufeld, T.P., de la Cruz, A.F.A., Johnston, L.A., and Edgar, B.A. (1998). Coordination of growth and cell division in the *Drosophila* wing. Cell *93*, 1183–1193.

72. Reddy, G.V., and Meyerowitz, E.M. (2005). Stem-cell homeostasis and growth dynamics can be uncoupled in the *Arabidopsis* shoot apex. Science *310*, 663–667.

73. Cosgrove, D.J. (2000). Loosening of plant cell walls by expansins. Nature *407*, 321–326.

74. Goh, H.H., Sloan, J., Dorca-Fornell, C., and Fleming, A. (2012). Inducible repression of multiple expansin genes leads to growth suppression during leaf development. Plant Physiol. *159*, 1759–1770.

75. Sloan, J., Backhaus, A., Malinowski, R., McQueen-Mason, S., and Fleming, A.J. (2009). Phased control of expansin activity during leaf development identifies a sensitivity window for expansin-mediated induction of leaf growth. Plant Physiol. *151*, 1844–1854.

76. Zhang, Y., Van de Peer, Y., Lu, B., Zhang, S., Che, J., Chen, J., Marchal, K., and Yang, X. (2023). Expression divergence of expansin genes drive the heteroblasty in *Ceratopteris chingii*. BMC Biol. *21*, 244.

77. Hydbring, P., Malumbres, M., and Sicinski, P. (2016). Non-canonical functions of cell cycle cyclins and cyclin-dependent kinases. Nat. Rev. Mol. Cell Biol. *17*, 280–292.

78. Lockhart, J.A. (1965). An analysis of irreversible plant cell elongation. J. Theor. Biol. *8*, 264–275.

79. Teleman, A.A., and Cohen, S.M. (2000). Dpp gradient formation in the *Drosophila* wing imaginal disc. Cell *103*, 971–980.

80. Randall, R.S., Sornay, E., Dewitte, W., and Murray, J.A. (2015). *AINTEGUMENTA* and the D-type cyclin CYCD3;1 independently contribute to petal size control in *Arabidopsis*: evidence for organ size compensation being an emergent rather than a determined property. J. Exp. Bot. *66*, 3991–4000.

81. Tsukaya, H. (2008). Controlling size in multicellular organs: focus on the leaf. PLoS Biol. *6*, e174.

82. Hong, L., DuMond, M., Tsugawa, S., Sapala, A., Routier-Kierzkowska, A.L., Zhou, Y., Chen, C., Kiss, A., Zhu, M., Hamant, O., et al. (2016). Variable cell growth yields reproducible organ development through spatiotemporal averaging. Dev. Cell *38*, 15–32.

83. Cockcroft, C.E., den Boer, B.G.W., Healy, J.M.S., and Murray, J.A.H. (2000). Cyclin D control of growth rate in plants. Nature *405*, 575–579.

84. Doerner, P., Jørgensen, J.E., You, R., Steppuhn, J., and Lamb, C. (1996). Control of root growth and development by cyclin expression. Nature *380*, 520–523.

85. Riou-Khamlichi, C., Menges, M., Healy, J.M., and Murray, J.A. (2000). Sugar control of the plant cell cycle: differential regulation of *Arabidopsis* D-type cyclin gene expression. Mol. Cell. Biol. *20*, 4513–4521.

86. Yang, L., Xu, M., Koo, Y., He, J., and Poethig, R.S. (2013). Sugar promotes vegetative phase change in *Arabidopsis thaliana* by repressing the expression of *MIR156A* and *MIR156C*. eLife *2*, e00260.

87. Yu, S., Cao, L., Zhou, C.M., Zhang, T.Q., Lian, H., Sun, Y., Wu, J., Huang, J., Wang, G., and Wang, J.W. (2013). Sugar is an endogenous cue for juvenile-to-adult phase transition in plants. eLife *2*, e00269.

88. Meng, L.S., Bao, Q.X., Mu, X.R., Tong, C., Cao, X.Y., Huang, J.J., Xue, L.N., Liu, C.Y., Fei, Y., and Loake, G.J. (2021). Glucose- and sucrose-signaling modules regulate the *Arabidopsis* juvenile-to-adult phase transition. Cell Rep. *36*, 109348.

89. Lawrence, E.H., Springer, C.J., Helliker, B.R., and Poethig, R.S. (2021). MicroRNA156-mediated changes in leaf composition lead to altered photosynthetic traits during vegetative phase change. New Phytol. *231*, 1008–1022.

90. Strauss, S., Lempe, J., Prusinkiewicz, P., Tsiantis, M., and Smith, R.S. (2020). Phyllotaxis: is the golden angle optimal for light capture? New Phytol. *225*, 499–510.

91. Carlson, M. (2019). org.At.tair.db: genome wide annotation for Arabidopsis. R package version 3.8.2.

92. Willis, L., Refahi, Y., Wightman, R., Landrein, B., Teles, J., Huang, K.C., Meyerowitz, E.M., and Jönsson, H. (2016). Cell size and growth

regulation in the Arabidopsis thaliana apical stem cell niche. Proc. Natl. Acad. Sci. USA *113*, E8238–E8246.

93. Eshed, Y., Baum, S.F., Perea, J.V., and Bowman, J.L. (2001). Establishment of polarity in lateral organs of plants. Curr. Biol. *11*, 1251–1260.

94. Curtis, M.D., and Grossniklaus, U. (2003). A gateway cloning vector set for high-throughput functional analysis of genes in planta. Plant Physiol. *133*, 462–469.

95. Pérez-Antón, M., Schneider, I., Kroll, P., Hofhuis, H., Metzger, S., Pauly, M., and Hay, A. (2022). Explosive seed dispersal depends on SPL7 to ensure sufficient copper for localized lignin deposition via laccases. Proc. Natl. Acad. Sci. USA *119*, e2202287119.

96. Schindelin, J., Arganda-Carreras, I., Frise, E., Kaynig, V., Longair, M., Pietzsch, T., Preibisch, S., Rueden, C., Saalfeld, S., Schmid, B., et al. (2012). Fiji: an open-source platform for biological-image analysis. Nat. Methods *9*, 676–682.

97. Tschumperle, D., and Deriche, R. (2005). Vector-valued image regularization with PDEs: a common framework for different applications. IEEE Trans. Pattern Anal. Mach. Intell. *27*, 506–517.

98. Ruifrok, A.C., and Johnston, D.A. (2001). Quantification of histochemical staining by color deconvolution. Anal. Quant. Cytol. Histol. *23*, 291–299.

99. Landini, G., Martinelli, G., and Piccinini, F. (2021). Colour deconvolution: stain unmixing in histological imaging. Bioinformatics *37*, 1485–1487.

100. Strauss, S., Runions, A., Lane, B., Eschweiler, D., Bajpai, N., Trozzi, N., Routier-Kierzkowska, A.L., Yoshida, S., Rodrigues da Silveira, S., Vijayan, A., et al. (2022). Using positional information to provide context for biological image analysis with MorphoGraphX 2.0. eLife *11*, e72601.

101. Ewels, P., Magnusson, M., Lundin, S., and Käller, M. (2016). MultiQC: summarize analysis results for multiple tools and samples in a single report. Bioinformatics *32*, 3047–3048.

102. Kim, D., Paggi, J.M., Park, C., Bennett, C., and Salzberg, S.L. (2019). Graph-based genome alignment and genotyping with HISAT2 and HISAT-genotype. Nat. Biotechnol. *37*, 907–915.

103. Anders, S., Pyl, P.T., and Huber, W. (2015). HTSeq-a Python framework to work with high-throughput sequencing data. Bioinformatics *31*, 166–169.

104. Robinson, M.D., McCarthy, D.J., and Smyth, G.K. (2010). edgeR: a Bioconductor package for differential expression analysis of digital gene expression data. Bioinformatics *26*, 139–140.

105. Babicki, S., Arndt, D., Marcu, A., Liang, Y., Grant, J.R., Maciejewski, A., and Wishart, D.S. (2016). Heatmapper: web-enabled heat mapping for all. Nucleic Acids Res. *44*, W147–W153.

106. Rohart, F., Gautier, B., Singh, A., and Lê Cao, K.A. (2017). mixOmics: an R package for 'omics feature selection and multiple data integration. PLoS Comput. Biol. *13*, e1005752.

107. Wu, T., Hu, E., Xu, S., Chen, M., Guo, P., Dai, Z., Feng, T., Zhou, L., Tang, W., Zhan, L., et al. (2021). clusterProfiler 4.0: a universal enrichment tool for interpreting omics data. Innovation (Camb) *2*, 100141.

108. Yu, G. (2022). enrichplot: visualization of functional enrichment result. R package version 1.16.2.

109. Wickham, H. (2016). ggplot2: Elegant Graphics for Data Analysis, Second Edition (Springer-Verlag).

110. Allen, M., Poggiali, D., Whitaker, K., Marshall, T.R., van Langen, J., and Kievit, R.A. (2019). Raincloud plots: a multi-platform tool for robust data visualization. Wellcome Open Res. *4*, 63.

111. Clough, S.J., and Bent, A.F. (1998). Floral dip: a simplified method for *Agrobacterium*-mediated transformation of *Arabidopsis thaliana*. Plant J. *16*, 735–743.

112. Shimada, T.L., Shimada, T., and Hara-Nishimura, I. (2010). A rapid and non-destructive screenable marker, FAST, for identifying transformed seeds of Arabidopsis thaliana. Plant J *61*, 519–528. https://doi.org/10.1111/j.1365-313X.2009.04060.x.

113. McDonald, K.L. (2014). Out with the old and in with the new: rapid specimen preparation procedures for electron microscopy of sectioned biological material. Protoplasma *251*, 429–448.

114. Moran, D.T., and Rowley, J.C. (1987). Biological specimen preparation for correlative light and electron microscopy. In Correlative Microscopy in Biology (Elsevier), pp. 1–22.

115. Reynolds, E.S. (1963). The use of lead citrate at high pH as an electron-opaque stain in electron microscopy. J. Cell Biol. *17*, 208–212.

116. Barbier de Reuille, P., Routier-Kierzkowska, A.L., Kierzkowski, D., Bassel, G.W., Schüpbach, T., Tauriello, G., Bajpai, N., Strauss, S., Weber, A., Kiss, A., et al. (2015). MorphoGraphX: a platform for quantifying morphogenesis in 4D. eLife *4*, 05864.

117. Usami, T., Horiguchi, G., Yano, S., and Tsukaya, H. (2009). The *more and smaller cells* mutants of *Arabidopsis thaliana* identify novel roles for *SQUAMOSA PROMOTER BINDING PROTEIN-LIKE* genes in the control of heteroblasty. Development *136*, 955–964.

118. Wagner, G.P., Kin, K., and Lynch, V.J. (2012). Measurement of mRNA abundance using RNA-seq data: RPKM measure is inconsistent among samples. Theory Biosci. *131*, 281–285.

119. Bassel, G.W., Stamm, P., Mosca, G., Barbier de Reuille, P.B., Gibbs, D.J., Winter, R., Janka, A., Holdsworth, M.J., and Smith, R.S. (2014). Mechanical constraints imposed by 3D cellular geometry and arrangement modulate growth patterns in the Arabidopsis embryo. Proc. Natl. Acad. Sci. USA *111*, 8685–8690.

120. Hofhuis, H., Moulton, D., Lessinnes, T., Routier-Kierzkowska, A.L., Bomphrey, R.J., Mosca, G., Reinhardt, H., Sarchet, P., Gan, X.C., Tsiantis, M., et al. (2016). Morphomechanical innovation drives explosive seed dispersal. Cell *166*, 222–233.

121. Mosca, G., Sapala, A., Strauss, S., Routier-Kierzkowska, A.L., and Smith, R.S. (2017). On the micro-indentation of plant cells in a tissue context. Phys. Biol. *14*, 015003.

122. Mosca, G., Eng, R., Adibi, M., Yoshida, S., Lane, B., Bergheim, L., Weber, G., Smith, R.S., and Hay, A. (2023). Growth and tension in explosive fruit. Preprint at bioRxiv.

STAR★METHODS

KEY RESOURCES TABLE

REAGENT or RESOURCE	SOURCE	IDENTIFIER
Antibodies		
Rabbit Anti-GFP antibody, polyclonal	Abcam	Cat# ab290; RRID: AB_303395
Rabbit IgG, polyclonal	Abcam	Cat# ab171870; RRID: AB_2687657
Bacterial and virus strains		
Escherichia coli (*E. coli*) DH5α	Lab stock	N/A
Escherichia coli (*E. coli*) DH10B	Lab stock	N/A
Agrobacterium tumefaciens GV3101 pMP90	Lab stock	N/A
Chemicals, peptides, and recombinant proteins		
½ MS Medium including vitamins	Duchefa Biochem	Cat# M0222.0050
Plant Preservative Mixture (PPM)	Plant Cell Technology	Cat# 250
BASTA®	Bayer Crop Science	Cat# 06470033
Hygromycin B	Carl Roth	Cat# CP12.1 CAS: 31282-04-9
5-Bromo-4-chloro-3-indolyl-β-D-glucuronide monohexyl ammonium salt (X-GlcA)	Carl Roth	Cat# 0018.3 CAS: 114162-64-0
Propidium Iodide (PI)	Invitrogen	Cat P1304MP CAS: 25535-16-4
4',6-Diamidino-2-phenylindole dihydrochloride (DAPI)	Sigma-Aldrich	Cat# D9542 CAS: 28718-90-3
Dexamethasone (DEX)	Sigma-Aldrich	Cat# D4902 CAS: 50-02-2
Cycloheximide (CHX)	Sigma-Aldrich	Cat# C7698 CAS: 66-81-9
PBS Tablets	Calbiochem (Millipore)	Cat# 524650
16% Formaldehyde Solution (w/v), Methanol-free	Thermo Fisher	Cat# 28908
Phenylmethylsulfonyl Fluoride (PMSF)	Calbiochem (Sigma-Aldrich)	Cat# 52332 CAS: 329-98-6
Protease inhibitor cocktail	Sigma-Aldrich	Cat# P9599
2-Mercaptoethanol	Sigma-Aldrich	Cat# M3148 CAS: 60-24-2
RNase Cocktail™ Enzyme Mix	Invitrogen	Cat# AM2286
Recombinant Proteinase K Solution	Invitrogen	Cat# AM2546
Critical commercial assays		
Mango Taq	Bioline	Cat# BIO-21083
KOD -Plus- Neo	Toyobo	Cat# KOD-401
NEBuilder HiFi DNA Assembly Master Mix	New England Biolabs	Cat# E2621
Araldite 502 and Embed 812 Kit	Electron Microscopy Sciences	Cat#13940
Quick CIP (calf intestinal alkaline phosphatase)	New England Biolabs	Cat# M0525
RNeasy Plant Mini Kit	QIAGEN	Cat# 74904
SuperScript® VILO™ cDNA Synthesis Kit	Invitrogen	Cat# 11754-050
Gateway™ LR Clonase™ II Enzyme Mix	Invitrogen	Cat# 11791-020
Power SYBR™ Green PCR Master Mix	Thermo Fisher	Cat# 4367659
Universal Plant ChIP-seq Kit	Diagenode	Cat# C01010152
NEBNext® Poly(A) mRNA Magnetic Isolation Module	New England Biolabs	Cat# E7490
Qubit™ dsDNA HS and BR Assay Kits	Invitrogen	Cat# Q32851

(Continued on next page)

Continued

REAGENT or RESOURCE	SOURCE	IDENTIFIER
Qubit™ RNA High Sensitivity (HS), Broad Range (BR), and Extended Range (XR) Assay Kits	Invitrogen	Cat# Q32852
TruSeq Stranded mRNA Library Prep Kit	Illumina	Cat# RS-122-2103
Deposited data		
RNA-seq dataset	This study	SRA-NCBI: https://dataview.ncbi.nlm.nih.gov/object/SRR24064950
A. thaliana Col-0 juvenile (leaf1) leaf time-lapse images (one-day time window, confocal stacks)	This study	Mendeley Data: https://doi.org/10.17632/69k277b76r.1
A. thaliana Col-0 adult (leaf8±1) leaf time-lapse images (one-day time window, confocal stacks) - Part I	This study	Mendeley Data: https://doi.org/10.17632/tvphv797m8.1
A. thaliana Col-0 adult (leaf8±1) leaf time-lapse images (one-day time window, confocal stacks) - Part II	This study	Mendeley Data: https://doi.org/10.17632/gcpptxtmy3.1
A. thaliana spl9spl15 mutant leaf8 time-lapse images (one-day time window, confocal stacks)	This study	Mendeley Data: https://doi.org/10.17632/6ky97vgnm5.1
A. thaliana pSPL9::SPL9r:Venus leaf1 time-lapse images (one-day time window, confocal stacks)	This study	Mendeley Data: https://doi.org/10.17632/chbrn423m7.1
A. thaliana pATML1::mTFP1:SPL9r leaf1 time-lapse images (one-day time window, confocal stacks)	This study	Mendeley Data: https://doi.org/10.17632/cc22z4z8bk.1
A. thaliana cycd3;1-3 mutant leaf8 time-lapse images (one-day time window, confocal stacks)	This study	Mendeley Data: https://doi.org/10.17632/z3jxvpndvf.1
2-hr time-lapse images (cellular growth dynamics during early development, i.e., 2-3 DAI, of *A. thaliana* leaf primordia, 2-hr time interval, confocal stacks)	This study	Mendeley Data: https://doi.org/10.17632/mhd99xr6sz.1
Arabidopsis reference genome TAIR10 release	The *Arabidopsis* Information Resource (TAIR)	TAIR: www.arabidopsis.org
Genome-wide annotation for *Arabidopsis*	Carlson[91]	Bioconductor: https://doi.org/10.18129/B9.bioc.org.At.tair.db
List of mitosis marker genes for the DMI calculation	Efroni et al.[36]	Table_S1_Marker gene list
Experimental models: Organisms/strains		
A. thaliana: Columbia ecotype (Col-0)	MPIPZ stock	N/A
A. thaliana: *spl9*	Schwarz et al.[18]	Peter Huijser, MPIPZ
A. thaliana: *spl9spl15*	Schwarz et al.[18]	Peter Huijser, MPIPZ
A. thaliana: *pSPL9::SPL9:Venus* (CN=2) / *spl9spl15*	This study	N/A
A. thaliana: *pSPL9::SPL9r:Venus* (CN=2) / *spl9spl15*	This study	N/A
A. thaliana: *pSPL9::SPL9r:Venus* (CN=10) / *spl9spl15*	This study	N/A
A. thaliana: *pSPL9::SPL9:Venus*	This study	N/A

(Continued on next page)

Continued

REAGENT or RESOURCE	SOURCE	IDENTIFIER
A. thaliana: pSPL9::SPL9r:Venus	This study	N/A
A. thaliana: pSPL9::NLS:miR156r:Venus	This study	N/A
A. thaliana: pATML1::mTFP1:SPL9r	This study	N/A
A. thaliana: pSPL9::SPL9:GUS	Xu et al.[12]	ABRC: CS69810
A. thaliana: 35S::SPL9r	This study	N/A
A. thaliana: pLMI1::SPL9r:Venus	This study	N/A
A. thaliana: pLMI1::CYCD3;1	This study	N/A
A. thaliana: pFAMA::SPL9r:Venus	This study	N/A
A. thaliana: pFAMA::3×Venus:NLS	This study	N/A
A. thaliana: pSPL9::SPL9r:GR (pSPL9::rSPL9r-GR)	Wang et al.[14]	Jia-Wei Wang, CEMPS
A. thaliana: cycd3;1-3	Dewitte et al.[63]	James A.H. Murray, Cardiff University
A. thaliana: spl9cycd3;1-3	This study	N/A
A. thaliana: pSPL9::NLS:miR156site: Venus / spl9	This study	N/A
A. thaliana: pSPL9::SPL9:Venus / spl9	This study	N/A
A. thaliana: pSPL9::CYCD3;2: miR156site:Venus / spl9	This study	N/A
A. thaliana: pSPL9::CYCD3;3: miR156site:Venus / spl9	This study	N/A
A. thaliana: pCYCD3;3::CYCD3;3: mCherry:3×Flag / spl9	This study	N/A
A. thaliana: pCYCD3;3mut::CYCD3; 3:mCherry:3×Flag / spl9	This study	N/A
A. thaliana: pCYCD3;3::CYCD3;3: mCherry:3×Flag / cycd3;1-3	This study	N/A
A. thaliana: pCYCD3;3mut::CYCD3;3: mCherry:3×Flag / cycd3;1-3	This study	N/A
A. thaliana: pUBQ10::PM:tdTomato	This study	N/A
A. thaliana: pUBQ10::PM:tdTomato / spl9	This study	N/A
A. thaliana: pUBQ10::PM:tdTomato / cycd3;1-3	This study	N/A
A. thaliana: pUBQ10::PM:tdTomato × pSPL9::SPL9r:Venus	This study	N/A
A. thaliana: pUBQ10::PM:YFP	Willis et al.[92]	Raymond Wightman, Uni. Cambridge
A. thaliana: pUBQ10::PM:YFP × spl9spl15	This study	N/A
A. thaliana: pUBQ10::PM:YFP × 35S::SPL9r	This study	N/A
A. thaliana: pUBQ10::PM:YFP × pATML1::mTFP1:SPL9r	This study	N/A
Oligonucleotides		
All Primers	This study	Table S1
Recombinant DNA		
Vector:pDONR221	Invitrogen	Cat# 12536017
Vector:pBJ36	Eshed et al.[93]	John L. Bowman, Monash University
Vector:pMDC32	Curtis and Grossniklaus[94]	ABRC: pMDC32 / CD3-738
Vector:pMLBart	TAIR	Vector:6530780616
Vector:pPZP200-FAST-RFP	Perez-Anton et al.[95]	Angela Hay, MPIPZ
Plasmid: pUBQ10::PM:YFP	Willis et al.[92]	Raymond Wightman, Uni. Cambridge
Plasmid: pLMI1-pBJ36	Vuolo et al.[53]	Miltos Tsiantis, MPIPZ
Plasmid: AtML1-pMDC32	Bilsborough et al.[48]	Miltos Tsiantis, MPIPZ
Plasmid: pMDC32-pSPL9	This study	N/A

(Continued on next page)

Continued

REAGENT or RESOURCE	SOURCE	IDENTIFIER
Plasmid: pMDC32-*p*SPL9::SPL9:Venus	This study	N/A
Plasmid: pMDC32-*p*SPL9::SPL9r:Venus	This study	N/A
Plasmid: pMDC32-*p*SPL9::NLS: miR156site:Venus	This study	N/A
Plasmid: pMDC32-*p*SPL9::NLS: miR156resistant:Venus	This study	N/A
Plasmid: pMDC32-*p*ATML1::mTFP1:gSPL9r	This study	N/A
Plasmid: pMDC32-*p*SPL9::CYCD3; 2:miR156site:Venus	This study	N/A
Plasmid: pMDC32-*p*SPL9::CYCD3; 3:miR156site:Venus	This study	N/A
Plasmid: pBJ36-*p*LMI1::SPL9r:Venus	This study	N/A
Plasmid: pMLBart-*p*LMI1::SPL9r:Venus	This study	N/A
Plasmid: pBJ36-*p*LMI1::CYCD3;1	This study	N/A
Plasmid: pMLBart-*p*LMI1::CYCD3;1	This study	N/A
Plasmid: pBJ36-*p*FAMA	This study	N/A
Plasmid: pBJ36-*p*FAMA::SPL9r:Venus	This study	N/A
Plasmid: pMLBart-*p*FAMA::SPL9r:Venus	This study	N/A
Plasmid: pBJ36-*p*FAMA::3×Venus:NLS	This study	N/A
Plasmid: pMLBart-*p*FAMA::3×Venus:NLS	This study	N/A
Plasmid: pPZP200-pFAST-RFP-*p*CYCD3; 3$_{mutated}$::CYCD3;3:mCherry:3×Flag	This study	N/A
Plasmid: pPZP200-pFAST-RFP-*p*AtCYCD3;3:: CYCD3;3:mCherry:3×Flag	This study	N/A
Software and algorithms		
Leica application suite X (LAS X)	Leica	https://www.leica-microsystems.com/products/ microscope-software/p/leica-las-x-ls/; RRID: SCR_013673
FIJI	Schindelin et al.[96]	https://imagej.nih.gov/ij/; RRID: SCR_002285
MorphoLibJ	INRA-IJPB Modeling and Digital Imaging lab (Arganda-Carreras and Legland)	https://imagej.net/plugins/morpholibj
Anisotropic Diffusion 2D	Tschumperle and Deriche[97]	https://imagej.nih.gov/ij/plugins/anisotropic-diffusion-2d.html
Colour deconvolution	Ruifrok and Johnston[98] Landini et al.[99]	https://blog.bham.ac.uk/intellimic/g-andini-software/colour-deconvolution-2/
MorphoGraphX (MGX version 2.0)	Strauss et al.[100]	https://www.MorphoGraphX.org
MorphoMechanX (MMX)		www.MorphoMechanX.org
MorphoDynamX (MDX)		www.MorphoDynamX.org
FFmpeg	FFmpeg Team	https://ffmpeg.org; RRID: SCR_016075
Leaf Interrogator (LeafI)	Zhang et al.[45]	GitHub: https://gitlab.mpcdf.mpg.de/g-adamrunions/ leafinterrogator_zhang_et_al
FastQC (Version 0.11.9)	Babraham Bioinformatics	https://www.bioinformatics.babraham.ac.uk/ projects/fastqc/; RRID: SCR_014583
MultiQC	Ewels et al.[101]	http://multiqc.info/; RRID: SCR_014982
HISAT (Version 2.2.1)	Kim et al.[102]	http://daehwankimlab.github.io/hisat2/; RRID: SCR_015530
HTSeq (Version 2.0)	Anders et al.[103]	https://htseq.readthedocs.io/en/ release_0.9.1/; RRID: SCR_005514

Continued

REAGENT or RESOURCE	SOURCE	IDENTIFIER
edgeR (version 3.38.4)	Robinson et al.[104]	Bioconductor: https://bioconductor.org/packages/edgeR; RRID: SCR_015687
Morpheus	Broad Institute	https://software.broadinstitute.org/morpheus/; RRID: SCR_017386
Heatmapper	Babicki et al.[105]	http://www.heatmapper.ca/; RRID: SCR_016974
mixOmics	Rohart et al.[106]	http://www.mixOmics.org; RRID: SCR_016889
clusterProfiler (Version 4.0)	Wu et al.[107]	Bioconductor: https://www.bioconductor.org/packages/clusterProfiler; RRID: SCR_016884
Enrichplot	Yu[108]	Bioconductor: https://www.bioconductor.org/packages/release/bioc/html/enrichplot.html
org.At.tair.db	Carlson[91]	Bioconductor: https://bioconductor.org/packages/release/data/annotation/html/org.At.tair.db.html
Digital Mitotic Index (DMI)	Efroni et al.[36]	N/A
Endoreduplication Index (EI)	Barow and Meister[52]	N/A
R (version 4.1.1)	R Core Team	www.r-project.org; RRID: SCR_001905
R package: ggplot2 (version 3.3.5)	Wickham[109]	https://ggplot2.tidyverse.org; RRID: SCR_021139
Raincloud	Allen et al.[110]	GitHub: https://github.com/RainCloudPlots/RainCloudPlots
Customised R scripts (2D growth alignment, cell division tracing, and combinelineages.r)	This study	GitHub: https://gitlab.mpcdf.mpg.de/sstrauss/r-analysis-for-li-et-al
Source codes for FEM modelling	This study	GitHub: https://gitlab.mpcdf.mpg.de/sstrauss/strain-based-growth-li-et-al.

RESOURCE AVAILABILITY

Lead contact
Further information and requests for resources and reagents should be directed to and will be fulfilled by the lead contact, Miltos Tsiantis (tsiantis@mpipz.mpg.de).

Materials availability
Genetic materials, including constructs and seeds, generated in this study have been deposited in the collections of the Department of Comparative Development and Genetics at the Max Planck Institute for Plant Breeding Research and will be made available upon request with a completed Materials Transfer Agreement (MTA).

Data and code availability

- RNA-seq data generated in this study have been deposited in the SRA-NCBI database and are publicly available as of the date of publication. Accession numbers are listed in the key resources table. All the time-lapse confocal data, encompassing long-term live-imaging (one-day interval) of leaves from various genetic backgrounds and leaf nodes, as well as high-resolution (2-hr time window) time-lapse stacks used for measuring cell cycle length, have been archived in Mendeley Data and are published alongside this paper. See the key resources table for DOIs of these datasets.
- For computational analyses of MGX data, including the 2D growth alignment, cell lineage tree construction for measuring cell cycle length, and lineage combination, the custom R scripts have been deposited at Gitlab and are publicly available as of the date of publication. DOIs are listed in the key resources table.
- Any additional information required to re-analyze the data reported in this paper is available from the lead contact upon request.

EXPERIMENTAL MODEL AND SUBJECT DETAILS

Bacteria and cultivation

Escherichia coli DH5α or DH10B was cultured at 37°C in LB medium for plasmid construction and amplification, with relevant antibiotics for selection. *Agrobacterium tumefaciens* GV3101, with a C58 chromosomal rifampicin resistance and the Ti plasmid pMP90 (pTiC58DT-DNA) gentamicin resistance, was cultured at 28°C for plant floral dip transformation.[111]

Plants and growth conditions

All *Arabidopsis thaliana* plants used in this study share the same Col-0 background. Genotypes are listed in the key resources table.

For soil-grown plants, seeds were sowed on pre-irrigated soil (mixture of 90% peat and 10% sand, long-term fertiliser contained, Balster Einheitserdewerk GmbH, Germany) surface and stratified for 3 days at 4°C in the dark. They were then moved to plant cultivation facilities (growth chambers or greenhouses) at the Max Planck Institute for Plant Breeding Research (MPIPZ) in Cologne, under the routine care of the professional gardener team. Plants were regularly irrigated with a nutrient solution (N:P:K ratio of 1.5:1:1.3), and beneficial nematodes (*Steinernema feltiae*), *Bacillus thuringiensis*, and several insecticides were applied as needed. Cork particles were laid on the soil surface ten days after seed germination to prevent gnat flies.

For phenotyping and quantitative analyses, plants were cultivated in walk-in chambers with fully-controlled climates (light intensity, 120 μmol·m^{-2}·s^{-1} for 8 hrs [short-day condition, SD]; relative humidity, 60%; temperature, 20°C/18°C day/night). For seed propagation, including for the genetic cross, transformation, and BASTA-resistance screen, plants were grown under long-day (16 hrs, LD) conditions in MPIPZ greenhouses, where artificial illumination was supplemented once the natural light intensity fell below 75 μmol·m^{-2}·s^{-1} during the daytime (temperature, 20 ± 2°C; relative humidity, 60 ± 10%).

To undertake screening for hygromycin-resistant plants, we sowed seeds upon ½ Murashige Skoog Basal Salt Mixture (MS) plates that contained 25 μg/mL hygromycin and 300 μl/mL cefotaxime following sterilization (50 % DanKlorix® for 10 min followed by four washes with ddH$_2$O). After this, we stratified the seeds at a temperature of 4°C, in a dark environment, for three days. Subsequently, these were grown within reach-in climatic chambers (Reftech) characterized by a relative humidity of 65% and a light intensity of 110 μmol·m^{-2}·s^{-1}. To identify seeds that contained the RFP seed coat marker,[112] we inspected such seeds under a fluorescence stereomicroscope (SMZ1500, Nikon), and those with moderate fluorescence were selected for further study. Any transgenic lines that were identified as positive were cultivated in a greenhouse with LD lighting conditions for the purposes of propagation. Alternatively, they were cultivated in walk-in chambers with SD conditions for phenotyping.

For time-lapse imaging, plants were grown on soil under LD conditions in the walk-in climatic chamber mentioned above for desired periods. Seedlings were then dissected to remove cotyledons (and older leaves for leaf8) and expose the target leaves for imaging. Dissected seedlings were placed in 5.5×1.5 cm Petri dishes containing ½ MS, 1.5% agar-agar, 1% sucrose and 1× plant preservative mixture (PPM, Plant Cell Technology) for confocal imaging. Afterwards, the samples were positioned upright in the plates without water and grown in reach-in climatic chambers (Reftech) under LD conditions until subsequent imaging (developing leaves were imaged every 24 hours for indicated days for growth analyses, and every two hours for cell cycle length measurement).

METHOD DETAILS

Plasmid construction and genetic materials

Genetic constructs were created using standard molecular cloning methods, including high-fidelity PCR (with KOD-Plus-Neo), conventional restriction enzyme digestion and ligation, and recombination-based seamless DNA assembly (Gateway cloning or NEBuilder). Newly cloned inserts were verified by Sanger sequencing, and all plasmids used in this study were fully confirmed by next-generation sequencing (Illumina).

For *SPL9* cloning, 3 kb upstream of the start codon of *SPL9* was amplified from *A. thaliana* genomic DNA (gDNA) with primers BamHI-pSPL9-F and KpnI-pSPL9-R and cloned into pMDC32 by *Bam*H I/*Kpn* I (pMDC32-*p*SPL9). The *SPL9* gene body was amplified from gDNA with primers KpnI-gSPL9-F and Linker-gSPL9-R, and the *Venus* tag was amplified using Linker-Venus-F and PacI-Venus-R. *SPL9* and *Venus* fragments were merged with a linker in-between by an overlap-extension PCR (KpnI-gSPL9-F/PacI-Venus-R) and finally cloned into pMDC32-*p*SPL9 with *Kpn* I/*Pac* I to produce pMDC32-*p*SPL9::SPL9:Venus. For the *p*SPL9::SPL9r:Venus construction, the miR156-resistant *SPL9* allele (*SPL9r*) was created by two rounds of mutagenic PCRs using the *p*SPL9::SPL9:Venus as template. The first DNA fragment was amplified using the primer combination KpnI-gSPL9-F/miR156rSPL9-R. The second DNA fragment was obtained with primers miR156rSPL9-F/PacI-Venus-R. These two fragments were spliced by an overlap-extension PCR with KpnI-gSPL9-F and PacI-Venus-R, and the merged fragment was cloned into pMDC32-*p*SPL9 with *Kpn* I/*Pac* I. For SPL9 transcriptional reporters, the KpnI-ATG-NLS-miR156site-Venus-PacI and KpnI-ATG-NLS-miR156resistant-Venus-PacI fragments were synthesized and cloned into pMDC32-*p*SPL9 via *Kpn* I/*Pac* I.

For *pLMI1::SPL9r:Venus* cloning, the SPL9r-Venus fragment was cloned from the *p*SPL9::SPL9r:Venus plasmid by PCR with NotIXmaI-SPL9-F/NotIXmaI-Venus-R, then cloned into *p*LMI1-pBJ36[53] via *Xma* I and moved into the destination vector pMLBart via *Not* I cloning. The mTFP1-linker-SPL9r was synthesized and cloned into pDONR221, then recombined into ATML1-pMDC32[48] via an LR reaction to make the *p*ATML1::mTFP1:SPL9r construct. The *FAMA* promoter (3,100 bp) was amplified from gDNA with PstI-pFAMA-F and XmaI-pFAMA-R primers and ligated into the intermediate vector pBJ36 (pBJ36-*p*FAMA). The SPL9r-Venus

cassette was cloned into pBJ36-*p*FAMA via the *Xma* I site, while the synthesized XmaI-3×Venus-NLS-BamHI was inserted into the same plasmid by *Xma* I/*Bam*H I double digestion. Then the *p*FAMA::SPL9r:Venus:OCSt or *p*FAMA::3×Venus:NLS:OCSt cassette was moved to the pMLBart binary vector through *Not* I cloning. For single restriction enzyme cloning (e.g., via *Xma* I or *Not* I), 5'-termini of linearized vectors were dephosphorylated (with calf intestinal alkaline phosphatase, CIP) to prevent vector self-ligation prior to target insertion.

For *CYCD3* genes cloning, the KpnI- Kozak site-CYCD3;2$_{CDS}$-linker-miR156site-Venus-PacI and KpnI- Kozak site-CYCD3;3$_{CDS}$-linker-miR156site-Venus-PacI cassettes were synthesized and cloned into pMDC32-pSPL9 via *Kpn* I/*Pac* I to obtain the bypass constructs (*p*SPL9::CYCD3;2:miR156site:Venus and *p*SPL9::CYCD3;3:miR156site:Venus, respectively); the CYCD3;1 genomic fragment was amplified from gDNA with XmaI-CYCD3-1-F/XmaI-CYCD3-1-R PCR primers and cloned into *p*LMI1-pBJ36.[53] With sequence and insert direction validated, the *p*LMI1::CYCD3;1:OCSt was moved into the unique *Not* I-site of pMLBart. For CYCD3;3 complementation, the BamHI-Linker-mCherry-Linker-3×Flag-XbaI fragment was synthesized and cloned into pBJ36 with *Bam*H I/*Xba* I (pBJ36-Linker-mCherry-Linker-3×Flag). The CYCD3;3 CDS was amplified from *p*SPL9::CYCD3;3:miR156site:Venus by PCR with primers KpnI-CYCD3;3CDS-F/BamHI-CYCD3;3CDS-R and cloned into the pBJ36-Linker-mCherry-Linker-3×Flag plasmid with *Kpn* I/*Bam*H I. The CYCD3;3$_{CDS}$-Linker-mCherry-Linker-3×Flag-OCSt fragment was then amplified from this plasmid with the primers CYCD3;3CDS-F/Flank3-OCS-R. The mutated CYCD3;3 promoter fragment was synthesized with all eleven GTAC elements converted into ATAT, then amplified with the Flank1-CYCD3;3p-F/Flank2-CYCD3;3p-R primers, while the CYCD3;3 natural promoter was cloned from gDNA with the same PCR primer pair. Finally, both (normal and mutated) promoters, the CYCD3;3$_{CDS}$-Linker-mCherry-Linker-3×Flag-OCSt fragment, and the *Bam*H I/*Pst* I double digested pPZP200-OLE1-RFP vector backbone were assembled with NEBuilder.

All constructs were transformed into corresponding plant lines using the floral dip method.[111] Transgenic lines were named after the transferred inserts, where the double colon refers to the promoter-gene relationship, and the single colon indicates an in-frame fusion of coding sequences (e.g., gene of interest, fluorescence reporter). For each construct, at least fifteen (usually 15-40) independent transformants were selected using the screening methods mentioned above. Independent transgenic lines were evaluated for phenotyping analyses, such as leaf morphometric assays. For *SPL9* expression quantification, 16 independent lines were analyzed for each translational reporter (*p*SPL9::SPL9:Venus or *p*SPL9::SPL9r:Venus/spl9spl15), and 3-5 representative *p*SPL9::SPL9:Venus lines, with the wild-type phenotype, were used for quantification. For time-lapse imaging, representative transgenic lines or relevant mutants were crossed to *p*UBQ10::PM:tdTomato or *p*UBQ10::PM:YFP, and homozygous descendants were used for cell outline detection. All transgenic lines used in this study were genotyped with transgene-specific primers (Table S1). Transgene copy number was determined with qPCR in dosage-dependent *SPL9* effects analysis (Figures 2A and S2A-S2D).

The *A. thaliana spl9* mutant used in this study is the *spl9-1* allele, which contains a 4-bp insertion in the first exon of *SPL9* resulting from the footprint left by the En-1 transposon.[18] This insertion causes a reading frame shift before the SBP-Box coding sequence and introduces a stop-codon 86-bp downstream. The *spl9spl15* mutant was generated by crossing *spl9-1* to *spl15-1* (SALK_074426),[18] which harbors a T-DNA insertion in the first intron of *SPL15* and eliminates its expression. The *cycd3;1-3* mutant is a triple mutant with one insertion in the first exon of each *CYCD3* gene (380-bp Ds insertions for *CYCD3;1* and *CYCD3;3*, 222-bp T-DNA insertion for *CYCD3;2*), resulting in null alleles of all three *CYCD3* genes.[63] The *spl9cycd3;1-3* quadruple mutant was generated by crossing *spl9-1* with *cycd3;1-3*. All mutants were genotyped using sequencing or molecular markers (see Table S1).

Microscopy and image analysis
Confocal microscopy (CLSM)
A Leica TCS SP8 confocal microscope was used for fluorescence imaging. Standard water objectives (AP 20×/0.80; AP 40×/0.50) were employed to image slide-mounted samples (e.g., cell outline imaging in mature leaves); whereas for in-plate imaging, especially the time-lapse tracing, long working-distance water immersion objectives (AP 20×/0.75; AP 40×/1.10; AP 63×/1.20) were used. For in-plate imaging, dissected plants were horizontally placed in the solid growth media mentioned above and immersed in ddH$_2$O containing 1× PPM during imaging. Fluorescence excitation was performed using an argon laser (20% output) or Diode Pumped Solid State lasers at relevant wavelengths with 458 nm for mTFP1 and chlorophyll auto-fluorescence; 514 nm for Venus, YFP, propidium iodide (PI), and chlorophyll; and 552 nm for tdTomato and PI. Emission signals were collected with a hybrid detector (HyD) or photo-multiplier (PMT, for PI and chlorophyll) detectors at 480-505 nm for mTFP1; 525-545 nm for Venus and YFP; 570-620 nm for tdTomato and PI; and 660-725 nm for chlorophyll auto-fluorescence.

For expression analyses, samples from the same set of experiments (e.g., *SPL9* translational reporter in different backgrounds) were imaged with the same settings to ensure their comparability. During reporter imaging, 1024×1024 resolution, 200 Hz, and 3-5 × line averaging were applied. For cellular growth analyses (with transgenic plasma membrane signal for cell outline imaging) where the fluorescence signal would not be compared quantitatively, settings (usually the gain, pinhole, and sometimes the laser intensity) for different samples were optimized for a good signal even during imaging (e.g., increase the gain value as the CLSM scans deeper layers during *z*-stacks). Additionally, for time-lapse imaging, confocal stacks were acquired at 512×512 resolution and a scanner speed of 400 Hz (bidirectional), 0.5-0.7 μm space between layers in the *z*-dimension, and without any averaging to minimize stressing plants. In normal time-lapse experiments, developing primordia or leaves were imaged daily, except that the last time interval in *p*SPL9:SPL9r:Venus imaging was two days, as the growth was highly repressed by *SPL9* overexpression. To measure the cell cycle length, samples were imaged every two hours over two days.

Scanning electron microscopy (SEM)

Plants were grown on soil under long-day conditions in walk-in climatic chambers. At 14 days after germination (DAG), seedlings were harvested, and the first seven leaves and cotyledons were removed. Fixation was conducted under vacuum in FAEG solution (4% Formaldehyde, 4% Acetic acid, 80% absolute Ethanol and 0.01% Glutaraldehyde) for 15 min. Samples were successively incubated in the FAEG solution and absolute ethanol (overnight at 4 °C for each incubation). Critical point drying was performed in absolute ethanol with 23 medium cycles at 37 °C, 1200 psi in EM CPD300 (Leica). Samples were arranged on metal platforms and sputter-coated with platinum using the EMS 7620 system (Leica). A Zeiss Supra 40VP scanning electron microscope was used for observations. Particular structures in the SEM images were artificially colored in Adobe Photoshop for visualization purposes.

Transmission electron microscopy (TEM)

To measure the cell wall thickness of the "proliferation burst" cell population, we collected leaf1 primordia two and three days after initiation (2 and 3 DAI, with a length of 100-150 μm and 250-350 μm, respectively). Samples were fixed at room temperature with 2.5% (v/v) glutaraldehyde and 2% (v/v) paraformaldehyde in 50 mM sodium cacodylate buffer (pH 6.9) supplemented with 0.025% CaCl$_2$ for two hours. Subsequently, samples were rinsed (three times for 10 min) in 50 mM sodium cacodylate buffer (pH 6.9), then postfixed in 0.5% osmium tetroxide and 0.15% potassium ferricyanide in 50 mM sodium cacodylate buffer (pH 6.9) for one hour at room temperature. After thorough washing with water (six times for 10 min), samples were dehydrated in a series of ethanol, gradually transferred to acetone and embedded into Araldite 502/Embed 812 resin using the ultrarapid infiltration by centrifugation method revisited by McDonald.[113] Samples were sectioned at the midline of the proximodistal axis (Figure S7D) into semithin slices (1 μm), stained with 1% aqueous toluidine blue supplemented with 1% sodium tetraborate and examined with a light microscope (Zeiss Axioscope A1, [Figures S7E and S7E']). Ultrathin (70-90 nm) sections were then collected on nickel slot grids as described by Moran and Rowley,[114] and stained with 2% aqueous uranyl acetate for 10 min and then Reynold's lead citrate[115] for 15 min. Images (Figures S7F and S7G) were taken with a Hitachi HT7800 TEM (Hitachi High-Technologies Europe GmbH, Krefeld, Germany) operating at 100 kV fitted with an emsis XAROSA 20-megapixel digital camera (EMSIS GmbH, Münster, Germany). The thickness of the outer walls of epidermal cells was measured with FIJI[96] and plotted in R (Figure S7G).

Cellular growth quantification

Cellular-level growth analyses and expression quantification were conducted using MorphoGraphX (MGX).[100,116] Confocal images were channel-split and converted into.tif format stacks using FIJI[96] before being loaded into MGX. When samples had to be imaged in part due to large size, adjacent image tiles were stitched together to form a complete stack in MGX. Stacks were processed following a standard pipeline to create curved surface segmentations and to track cell lineages (see the MGX user guide for details).[116] Briefly, the global shape of the sample was extracted with Gaussian blur and the edge detection process, and a curved organ surface (2.5D) mesh was generated using marching cubes. The cell outline signal (cytomembrane-located fluorescence or PI-stained cell wall signal) from the epidermal layer (2-6 μm from the surface) was then projected onto the surface mesh for cell segmentation. For each leaf primordium, half (from medium line to edge) of the abaxial epidermis was analyzed as the proxy of the entire leaf. The target regions or cell types in different samples were carefully defined according to consistent standards (e.g., their position or morphological features) to guarantee sample comparability.

Based on well-refined cell segmentation, cell geometry was measured in MGX, including:

- Cell area - as a proxy of cell size in 2.5D. E.g., in (Figure S1B).
- Cell lobeyness - the ratio of a cell's perimeter over that of its convex hull; a higher value indicates a more complex cell shape, i.e., higher pavement cell differentiation.[42] E.g., in (Figure 4D).

The parent-daughter relationships (lineage maps) of cells between successive time points were created manually in MGX. Parental relationships over various time windows (i.e., spanning various observation periods) were then computed by linking those successive lineages with a custom R script, excluding incomplete lineages (combinelineages.r, see the key resources table).[33] A full-lineage cell fate map was constructed after manual correction, enabling cellular growth and development tracing. Growth over a given period was computed as follows:

- Proliferation: the number of cells originating from a single cell after a given period. e.g., in (Figure 1E).
- Growth rate: also called "area extension", the ratio of the area of a single cell-originated clonal sector after a given period of growth, to that of the original cell (fold change). e.g., in (Figure 1H).
- Cell area change: the difference between the original cell area and the average area of progeny cells after a period, computed by dividing the area extension by the proliferation in a specific single cell-originated sector (e.g., in Figure 1F). The value "1" indicates that the cell area remains the same and that growth is associated with cell number increase (i.e., proliferation); a higher value (dark green in heatmaps) indicates a larger increase in cell area (usually reflecting cell expansion); while smaller values (purple) indicate a decrease in cell area, associated with more pronounced increase in cell number than cell area (reflecting high proliferation).
- Growth anisotropy: the ratio of maximum to minimum stretch of a clonal sector of one cell, where stretch means the ratio of the length of the clone to that of the original cell along the maximum/minimum Principal Directions of Growth (PDG). The PDG was computed according to the relative positions of cell junctions,[116] which were identified by the cell lineage information.

Anisotropy equal to one means the growth is isotropic. The maximum PDG was visualized as white lines in cells where the anisotropy was above an indicated threshold. E.g., in (Figure 1I).

- PD and ML growth: the growth rate (length stretch, the ratio of the length of a clone to that of its source cell) along proximodistal (PD) or mediolateral (ML) directions. The organ coordinates (PD-ML) were created based on the Euclidean distance field in the PD direction (Figure 1J), for which the basal cell line was selected as the reference position and the Euclidean distance was determined by finding the shortest paths from cells in the leaf to the reference cells. The PD axis is defined along the Euclidean distance gradient (Figures S1G and S1H), while the ML axis is the perpendicular direction along the leaf surface (Figure S1I). Both directions follow the organ's natural curvature. The amount of growth along these directions was determined using the PDGs (mentioned above). Because the Euclidean distance-based coordinates change during growth, PD and ML growth measured based on the start coordinates would not fit well with the end coordinates. Therefore, we usually visualized PD or ML growth on the start time point of the measure (e.g., Figures S1H and S1I). When projecting PD or ML growth on the last mesh (e.g., Figure S3D), we re-established the coordinates with a Bezier line[100] along the PD axis to minimize the effects of coordinate changes.
- PD/ML ratio: the ratio of growth (elongation) along the PD axis to that along the ML axis over a given period. As a parameter derived from PD and ML growth, the PD/ML ratio is visualized in the same way, i.e., on the coordinates mesh (start mesh, e.g., Figure S1E) or the end mesh with Bezier-adjusted coordinates (e.g., Figure 1J).

All cellular data obtained with MGX were exported to CSV files and further analyzed using R. Biological replicates were included for every leaf type, and each replicate represents a single time-lapse experiment with varying observation periods (e.g., among the four replicates for Col-0 leaf1, two samples were imaged from 1-6 DAI, while the other two were imaged from 1-5 DAI). An exception is Col-0 leaf8, where each biological replicate represents a full developmental series composite of early (1-3 DAI) and late (2-6 DAI) observations with an overlapping window of two time points (2-3 DAI). Due to these varying observation periods among replicates, and the overlapping periods used for the Col-0 leaf8 analysis, the numbers of data points can vary over time in the temporal analysis datasets.

In addition to statistical quantification using replicates, measures from representative replicates were visualized as heatmaps. The representative time-lapse series were selected without bias, as those with the lowest RMSE (Root Mean Square Error) from the regression of all samples. Heatmaps of different measures were generated in MGX, and snapshots of different leaves (variant time points and genotypes) were stitched in Photoshop (note that the Col-0 leaf8 series is a composition of early [1-3DAI] and late [3-6 DAI] samples). Cell geometry (cell area, lobeyness) was visualized on the measuring mesh, while time-lapse growth between two time points was projected on the later mesh unless mentioned otherwise.

Cell cycle length was computed using cell lineage data (CSV files exported from the MGX) over 18 time points (after an adaptation period of the first four time points) with a 2-hr time-window. A custom R-script was developed to build a lineage tree of the descendants of all cells from the initial time points (see the key resources table). Next, cell division events were determined. We calculated the cell cycle length for all cells with at least two divisions by computing the time interval between the division events.

Growth animation

To depict the developmental dynamics of cellular lineage and growth, videos (Videos S1, S2, and S3) were generated using MGX[100] and FFmpeg (https://ffmpeg.org). First, the frames of the animated meshes were acquired in MGX by implementing the morphing animation feature. Subsequently, the videos were compiled from the individual frames in FFmpeg. Following the cropping and arrangement of various genotypes, explanatory annotations were incorporated, and the final outputs were exported in the MP4 format.

Growth alignment

To quantitatively compare cellular growth and developmental contributions over time between different genotypes with biological replicates, we mapped cellular growth characteristics according to their locations or identities in various alignment approaches.[33,45,100]

Organ coordinate-based alignment

Different leaves were aligned according to their PD/ML coordinates mentioned above, where cells were annotated with relative positional information (normalized by leaf primordium length to compensate for their size variations).[45,100] Cells were binned by their Euclidean distances from the leaf base (binning along the PD axis) or the midrib (ML binning) such that each bin had approximately the same number of cells (cellular binning or ordinal binning), the same area (areal binning), or the same length along the specified axis (Euclidean binning).

This binning was propagated by cell lineage to later time points, allowing the growth of each bin to be quantified. The average cellular quantification for each bin was calculated and plotted against the relative coordinate system. For growth between time points (e.g., Figures S1J1-S1K7), the measures were plotted according to the coordinates of the starting primordia.

For PD alignment (one-dimensional alignment, e.g., Figures S1J1–S1K7 or S3A1–S3A3), cellular quantifications or time-lapse growth over corresponding periods were binned using the ordinal binning method (each bin contains an equivalent number of cells) and aligned by the Euclidean distance from the leaf base.

For growth contribution to leaf development (proportional growth) between two time points, two-dimensional (2D, or PD-ML) alignment was applied (e.g., Figures 1N and 1P). In this case, cells at the first time point were binned along the PD and ML axes

simultaneously by their respective Euclidean distances from the base and midrib of the leaf (Figure S1M), and the binning information was propagated to the second time point via the parental lineages. The cell number or area of each bin at the first time point (Euclidean binning effect) was normalized afterwards. Growth contribution was defined as the relative contribution of each bin to the cell number (cellular contribution) or the area (areal contribution) of developing leaves over a given period. These were in turn calculated as the relative changes in the proportion of cells/areas in the whole leaf after a period of growth. For example, we calculated the cellular contribution (CC) of a bin at time point 1 to the developing leaf at time point 2 in this way:

$$CC = \frac{P_2}{P_1}$$

where P_1, P_2 are the proportions of interested cells (cells in a specific bin) out of the total cells of the leaf at time points 1 and 2, respectively. e.g.,

$$P_1 = \frac{C_{bin1}}{C_{total1}}$$

Here, C_{bin1} is the number of cells in the bin, and C_{total1} is the total number of cells in the whole leaf, at time point 1. As incomplete lineages were removed before the calculation (with the combinelineage.r script, see the key resources table), all cells analyzed here refer to cells with complete lineages between the two time points.

The same formula was applied for the calculation of P_2, with the binning information inherited from time point 1 according to cell lineage.

For the areal contribution calculation, cell area instead of cell number was used in the same formula.

Growth contributions were normalized and converted into percentages and the average contribution of each bin with biological replicates was plotted in the PD/ML coordinate. Additionally, we computed the weighted mean of growth contribution in normalized PD/ML coordinates directly from the cellular data. The weighted mean positions of different replicates were plotted to compare different leaf growth patterns (e.g., Figure 2E).

Cell type-based alignment
To reveal the growth divergence among different developmental domains, we tracked leaf development in four distinct lineages: margin, midrib-petiole, distal blade, and proximal blade (Figure 1C). Cells were classified according to their geometrical features and growth properties at the last time point: margin was defined as the elongated giant cells along the leaf edge; midrib-petiole was composed of the petiole cells and their midrib continuation with similar cell shape (long cells with high aspect ratio but low lobeyness) and growth anisotropy (elongated along the PD axis); the rest (blade) was delimited into distal and proximal blades with approximately the same length along the PD axis. These cell types were mapped to earlier time points using backward lineage tracing. Cellular quantifications and time-lapse growth measures in each cell type were summarized with biological replicates and compared among different growth patterns in heatmaps (e.g., Figures S1L1–S1L4) or plots (e.g., Figure 2H). Representative sectors of different cell types were tracked and shown in lineage maps (e.g, Figures S1N and S1O).

As a functionally specified cell type, stomata were used to indicate tissue differentiation in leaf development (e.g., Figures 4G-4I). Stomata were identified with an MGX plugin - "visibility stomata",[42] followed by manual correction according to their kidney-shaped morphology. Because the guard mother cell (GMC) division showed different proliferation dynamics from other blade cells, the stomata-yielding divisions were labelled specifically in the cell-cycle measure analysis (Figure 2F).

Expression analysis
Confocal imaging and quantification
To examine *SPL9* expression, we imaged corresponding fluorescence signals (Venus or mTFP1) with CLSM using consistent settings. For *SPL9* spatiotemporal expression examination (e.g., Figures 3A and 3B), only *pSPL9::SPL9:Venus* lines without gain-of-function phenotypes were chosen, to avoid potential effects from transgene-introduced over-expression. To quantify *SPL9* expression in the epidermal layer, signals from 2-6 μm away from the surface were projected onto a surface mesh with MGX (e.g., Figure 3A). For PD alignment of *SPL9* expression, a Bezier line along the leaf midrib was created as the PD axis. The Bezier line was then divided into ten segments of equal length, which acted as bins; the surface mesh was divided according to these bins, and the sum of the surface signal from each bin was normalized by bin area and plotted as a function of the distance from the leaf base (Figure 3B), in the same way as was performed for PD growth alignment.

GUS staining
Plants were grown under short-day conditions in walk-in chambers until the desired stages were reached. Aerial parts of plants were harvested into ice-incubated 90% acetone (v/v) and fixed for 30 min at room temperature. Before β-Glucuronidase (GUS) staining, samples were washed three times on ice with staining buffer (2mM $K_4Fe(CN)_6$, 2mM $K_3Fe(CN)_6$, 10mM EDTA, and 0.1% Triton X-100 (v/v) in 50mM phosphate buffer, pH 7.2). Then samples were moved to pre-cooled GUS staining solution (1 mM 5-bromo-4-chloro-3-indolyl-β-D-glucuronic acid [X-Gluc, Roth, dissolved in N, N-Dimethylformamide] in the staining buffer) and infiltrated on ice under vacuum until all samples sank to the bottom. The staining reaction took place at 37°C in the dark for 10 hours. After incubation, the reaction solution was replaced by 20%, 50%, 70%, and 90% ethanol (v/v) sequentially. For solution displacement, samples were incubated in each new solution for 3 hours on a shaker. Samples were then dissected under a stereomicroscope (Nikon SMZ1500) and imaged using a Zeiss Axio Imager M2 light microscope (for small samples) or Zeiss Smartzoom 5 digital microscope

(large samples). To improve the comparability and visibility of the GUS staining in transmitted light RGB images, we performed a color deconvolution in FIJI,[96] as described by Ruifrok and Johnston[98] and implemented by Landini et al.[99] The deconvolved GUS color was then recombined with the luminosity level of the original image. For ease of comparison, the images were white-balanced and their backgrounds were offset to an equivalent level.

RT-qPCR

Plant materials were prepared as described for RNA-seq sampling. For SPL9 inducible activation assays using *pSPL9::SPL9r:GR*, Cycloheximide (CHX, a protein synthesis inhibitor in eukaryotes, final concentration 40 μM) was added in both treatment (along with 30 μM DEX) and control solutions to estimate SPL9's direct effects on transcription (without new protein synthesis). Total RNA was extracted with the RNeasy Plant kit (QIAGEN) with DNase I on-column treatment. RNA quantity and quality were measured with a spectrophotometer (NanoDrop® ND1000, PEQLAB) and 2.5 μg diluted in 14 μl RNase-free H_2O was directly used for cDNA first strand synthesis with SuperScript VILO reaction mix (Invitrogen). The concentration of cDNA was measured again with a NanoDrop® ND1000, and samples were diluted for subsequent quantitative PCRs. Real-time qPCR was performed in QuantStudio 3 Real-Time PCR System (Applied Biosystems) using PowerSYBR® Green PCR Master Mix (Applied Biosystems) with ROX as passive reference according to the manufacturer's instructions and with reactions scaled down to 20 μl. To minimize technical variation and contaminations among samples, we used low-binding pipette tips with leak-proof tops (Santa Cruz Biotechnology, EZ Touch Barrier Pipette Tips) for sample loading and distributing. The amplification efficiencies of all primers used for quantitative PCR (see Table S1) were determined (90-100%). β-tubulin 2 (AT5G62690) was used as the internal reference[14] for relative quantification with $2^{-\Delta\Delta CT}$ calculation.

Mature leaf quantification

Leaf morphometric study

Fully expanded rosette leaves were obtained from short-day grown plants, flattened onto white paper with a transparent adhesive sheet, and scanned at 800 dpi resolution to generate leaf silhouettes. Digital silhouettes were then analyzed with Leaf Interrogator (LeafI)[45] according to the user guide. First, silhouettes were identified and converted into vector contours (sequences of 2D positions). Leaf contours were then anchored with two common landmarks at the tip and base and resampled to have 120 points on each side, equally spaced (i.e., arc-length parameterized). General geometrical quantifications of leaves were performed on these contours. Leaf shape spaces were created by analyzing the resampled leaf contours with a combination of the Procrustes-Based alignment and Elliptical Fourier Descriptor (EFD) method, which eliminates confounding variations of rotation, translation, and scale to display bilaterally symmetrical leaf shapes. Size-invariant shape analysis was performed with Principal Component Analysis (PCA) on the first 64 harmonics of the Fourier coefficients. The first principal component (PC1) accounted for the majority of variance in all cases and correlated very well with leaf node (Figure 2A). This indicates that it captured most of the age-dependent leaf shape variation, and thereby, could be a good proxy for leaf heteroblasty. Statistical summaries computed from the spectral decomposition of each group's covariance matrix were plotted with samples in shape spaces (e.g., Figures 2A, 6A′, and 6D), and further visual inspections of these models allow for interpretation of the PCA results. The results (e.g., area, eccentricity, PC1 as multiples of its standard deviation in each group) were also exported as.csv files, and analyzed and visualized, e.g., as heatmaps (Figures 1A and 6A) or plotted in R (Figure S2D).

Total cell number estimation

Fully expanded leaves were harvested from short-day grown plants and placed on microscope slides before CLSM imaging of plasma membrane markers, as described above.

To determine the cellular effects of SPL9 on final leaf size, we quantified subepidermal cells as a proxy (Figures S2F and S4F). Compared to epidermal cells, subepidermal (palisade mesophyll) cells are uniform in shape and transverse area in mature leaves,[117] which makes them more suitable for inter-genotype comparisons.

For each leaf, four uniformly distributed regions were imaged. Confocal stacks were loaded into FIJI[96] and segmented based on the MorphoLibJ and Anisotropic Diffusion 2D plugins.[97] After image contrast improvement (reducing background noise while preserving sharp edges), a binary cell outline image was generated with Watershed lines. Cells were then measured after manual correction to remove those wrongly segmented cells and air pores (fake cells). Areas of around 200-400 cells (more cells were measured at higher leaf nodes) were measured for each leaf and averaged. Seven individual leaves were examined for each genotype. For total cell number estimation, we first calculated the cell density of observed regions, then multiplied the average cell density of a leaf by the total area of that leaf.

Ploidy analysis

Plants were grown on soil under long-day conditions in walk-in climatic chambers for relevant periods (until target leaf primordia were approximately 5 mm in length). Leaves were then harvested, chopped with a razor blade, and resolved in Galbraith Buffer (45 mM MgCl2, 30 mM sodium citrate, 20 mM MOPS, 0.1% (v/v) Triton X-100, pH 7.0). Debris was removed with 30 μm CellTrics® filters (Sysmex), and nuclei were stained with 0.1% DAPI for 20 min on ice. Polyploidy was analyzed with the CytoFlex system (Beckman-Coulter). Peaks were assigned manually, and automatic quantification was performed with the CytExpert software. The endoreduplication index (EI, Figures 5A and 5C) was calculated according to the previous "cycle value"[52] estimation:

$$EI = 0 \cdot \%_{2C} + 1 \cdot \%_{4C} + 2 \cdot \%_{8C} + 3 \cdot \%_{16C} + 4 \cdot \%_{32C}$$

Where $\%_{2C}$, $\%_{4C}$, $\%_{8C}$, $\%_{16C}$, $\%_{32C}$ (plotted in Figures S5A and S5A′), are the proportions of indicated nucleus groups in the total population of nuclei analyzed, e.g.,

$$\%_{2C} = \frac{n_{2C}}{n_{2C}+n_{4C}+n_{8C}+n_{16C}+n_{32C}}$$

n, the number of nuclei with the corresponding C-value (2C, 4C, 8C,...), which indicates the DNA content per nucleus (1C corresponds to the mass of DNA present in a gamete).

Transcriptome analysis
RNA-seq experiment
Plants were grown on soil under short-day conditions in walk-in chambers for relevant time periods:

1) For the leaf series at different leaf nodes: Col-0 leaf2, 5, 7, and 9 were harvested when they were around 5 mm in length. Apices with establishing primordia were also harvested seven days after sowing.
2) For the leaf5 maturation series: Col-0 leaf5 was collected at around 1mm, 5mm, 2cm, and at a fully expanded stage.
3) For transcriptomes of different genotypes (Col-0, *spl9*, *pSPL9::SPL9r:Venus/spl9spl15*): young leaf primordia (from leaf5 on, including the shoot apex) were collected when leaf5 was visible (about 5 mm in length).
4) For Dexamethasone (DEX) treatment: two-week soil-grown *pSPL9::SPL9r:GR* plants were sprayed with DEX (30 μM with 0.02% Silwet L-77) or mock solution every hour. Young leaf primordia (leaf5-to-apex) were collected 4 hours after the first spray.

For each transcriptome (genotype, leaf type, or treatment), at least ten individual plants were pooled for each of three biological replicates. All samples were snap-frozen in liquid nitrogen immediately after harvesting. Samples were then ground for 100 sec at 30 Hz in a TissueLyser tissue mill (QIAGEN) with pre-cooled racks. Total RNA was purified using the RNeasy Plant kit (QIAGEN) with On-Column DNase digestion performed.

RNA samples were quantified with a Qubit 2.0 RNA HS assay (Thermo Fisher Scientific Inc.), and their qualities were evaluated using the RNA ScreenTape on a Tapestation (Agilent Technologies Inc.). High-quality RNA samples were then sequenced at Admera Health LCC (South Plainfield, NJ, USA). Message RNAs were enriched by poly(A) selection. Total RNA was incubated with oligo d(T) 25-coupled paramagnetic beads to isolate poly(A)+ transcripts (NEBNext® Poly(A) mRNA Magnetic Isolation Module). The library was then constructed using a TruSeq stranded mRNA library kit (Illumina), followed by quantification (Qubit 2.0, ThermoFisher) and quality control (QC, TapeStation D1000 ScreenTape, Agilent Technologies Inc). The average fragment size was about 500 bp, with an insert size of about 350 bp in final libraries. Illumina® 8-nt unique dual indices were exploited. Libraries were equimolarly pooled according to their QC values and sequenced on an Illumina® NovaSeq S4 with a read length configuration of 150 bp paired-end (PE) for 40 million PE reads per sample (20 million in each direction).

DEG
RNA-seq raw data quality was first checked by FastQC and summarized by MultiQC.[101] All transcriptomes showed high sequencing quality, except for reads from one direction of a Col-0 replicate. This Col-0 replicate was then treated as a single-end sequencing sample in further analyses. Sequencing reads were then mapped to the reference genome TAIR10 for *A. thaliana* using HISAT 2.2.1[102] with default settings. The outputs were sorted by name, and gene-associated reads were quantified with HTseq-count.[103] Gene expression was determined in transcripts per million (TPM)[118] and differentially expressed genes (DEG) were tested by edgeR.[104] SPL9-responsive genes were identified as a gene set with reciprocal responses to *SPL9* loss- and gain-of-function. Specifically, the overlap between up-regulated genes in the *pSPL9::SPL9r:Venus/spl9spl15* transcriptome and down-regulated genes in *spl9* compared to wild-type was defined as SPL9-activated genes, whereas genes down-regulated in *pSPL9::SPL9r:Venus/spl9spl15* while showing higher expression in *spl9* relative to the wild-type were defined as SPL9-repressed (Figure S5H). The expression patterns of these two gene sets (normalized expression) in different leaf nodes or during leaf maturation were confirmed (Figures S5J and S5J′). Hierarchical clustering and heatmap analysis of SPL9-responsive genes (Figure S5K) were performed using Heatmapper.[105]

Enrichment analyses
GO. Gene Ontology enrichment analyses[60,61] were performed on SPL9-activated and -repressed gene sets separately with clusterProfiler.[107] Biological process (BP, level = 3) and cell component (CC) enrichment were examined with the parameters "pvalueCutoff = 0.01, pAdjMethod = "BH", qvalueCutoff = 0.05, showCategory=15" in the enrichGO() function. CC enrichment results were exclusively chromosome or chloroplast-harboured structures in SPL9-activated and -repressed gene sets, respectively (summarized as illustrations in Figure S5K).

GSEA. Gene Set Enrichment Analysis[58] was performed to evaluate the distribution of representative cell cycle-related gene ontology items (GO:0022402, cell cycle process; GO:0007059, chromosome segregation; GO:0006310, DNA recombination; GO:0044772, mitotic cell cycle phase transition in Figures 5F, S5E, and S5E′) and cell growth-related processes (GO:0016049, cell growth; GO:0009826, unidimensional cell growth; GO:0060560, developmental growth involved in morphogenesis in Figures S7A and S7B) in relevant transcriptomes. The clusterProfiler[107] was exploited with the parameters "minGSSize = 50, maxGSSize = 500, pvalueCutoff = 0.05" in the gseGO() function. Normalized enrichment score (NES) and the statistical significance

of the enrichment (false discovery rate, FDR) were provided with the running enrichment plot and gene ranking positions (horizontal lines at the bottom) in the indicated comparison. The same method was employed to assess the distribution of SPL9-activated and -repressed genes in the SPL9-induced transcriptome (Figures S5I and S5I′).

DMI
Digital Mitotic Index (DMI) was computed as a transcriptomic estimation of tissue proliferation level.[36] The expression of mitotic marker genes from a previously reported gene set[63] was normalized as the ratio between the mean TPM in an indicated transcriptome and the maximal mean TPM among samples analyzed. The DMI was plotted in R (Figures 5E and S5D).

sPLS-DA
Partial Least Squares (PLS) is a dimensionality reduction method calculating new dimensions that maximize the covariance between dependent (different developmental stages in this study) and independent variables (gene expression levels here), in comparison to other dimensionality reduction methods such as PCA (Principal Component Analysis) that try to maximise the variance between different independent variables. In other words, PLS creates its new composite variables (latent factors) to explain the largest variability in the response of the explanatory variables to a dependent variable. It is especially useful when there is a small number of samples with a lot of features (genes, in this case), because the small number of samples elevates the multi-collinearity problem between the genes. PLS-DA (PLS Discriminant Analysis) is an extension of the PLS method used when the dependent variable is discrete, as is the case in our analyses (e.g., leaf nodes). The sparse version of PLS (sPLS) was used for categorical variables classification or biological feature selection using gene expression matrices.[59] sPLS-DA with RNAseq data from developmental time-series ensures that the first latent factors summarize the expression of genes that show a response along the time-series; which is not necessarily the case using PCA. Therefore, the latent components of PLS have a significant meaning while predicting the dependent variable (developmental stages in our case) as a supervised model. Here, using sPLS-DA, we first derived the reduced representation of two developmental series with training/calibration samples, then projected the test samples (transcriptomes disturbed by *SPL9* manipulation) on top of the models. By not including the test samples in the construction of the models, we ensured that the latent factors only represent sets of genes varying with the developmental series, and are not affected by potential effects of *SPL9* perturbation or tissue heterogeneity.

In this study, the classes of calibration samples represent leaf developmental stages at two distinct scales, i.e., during shoot ageing (calibration series 1, age of the plant) or leaf maturation (calibration series 2, age of the leaf); consequently, the first latent variables of the sPLS-DA models represent pseudo-time trajectories in these two developmental directions and could effectively predict the developmental stage of test samples.

- Calibration series 1: *A. thaliana* wild-type (Col-0) leaves at different leaf nodes. Leaf2, 5, 7, and 9 were harvested when they were around 5 mm in length. The apex samples with emerging primordia, collected seven days after sowing, were used as the starting point of leaf development with very low differentiation.
- Calibration series 2: *A. thaliana* wild-type (Col-0) leaf5 maturation series. Leaf5 samples were collected at around 1 mm, 5 mm, 2 cm, and fully mature stages.
- Test Samples: SPL9-modulated transcriptomes (genetic perturbation: *pSPL9::SPL9r:Venus/spl9spl15*, *spl9*, versus Col-0, or chemical induction: DEX/mock-treated *pSPL9::SPL9r:GR*). Developing leaf primordia (< 5 mm) were collected with the apex.

Analyses were conducted using the **splsda** function of the mixOmics R package[106] with the 1000 genes (features, set by the keepX function) showing the largest variance in expression. Dimensionality reductions were done using the calibration sets only and were visualized with the first two latent variables. The number of clusters was specified by k means. The centroids of all the clusters were calculated, and the closest centroids were connected to each other by calculating the Euclidean distance between centroid pairs, to build a pseudo-time developmental trajectory. Test samples (SPL9-modulated transcriptomes) were then projected onto the model. The positions of these samples in the sPLA-DA plot represent their relative developmental stages (Figures 5G, S5F, S5G, and S5G′). In this way, the transcriptomic effects of SPL9 on age-dependent leaf development were evaluated.

ChIP experiment
Chromatin immunoprecipitations were performed with a universal plant ChIP-seq kit (Diagenode) according to its manual with some modifications. Homozygous *pSPL9::SPL9r:Venus/spl9spl15* and *pSPL9::miR156r:Venus* transgenic plants were grown on soil under short-day conditions, as mentioned above, for around one month. The aerial parts were collected on ice in three groups: the experiment group, *pSPL9::SPL9r:Venus/spl9spl15* treated with anti-GFP antibody (ab290, Abcam); the antibody control group, the same plant line *pSPL9::SPL9r:Venus/spl9spl15* treated with Non-Immune control immunoglobulin (IgG, ab171870, Abcam); and the plant control group, *pSPL9::miR156r:Venus* with the same anti-GFP antibody (ab290, Abcam). At least three replicates (1-2 grams of fresh tissue per replicate) were sampled for each group.

Mature leaves (leaf 1-4) were removed; the rest were cleaned and cross-linked in a Crosslinking Buffer containing 1% formaldehyde under a vacuum for 3× 10 min on ice. The cross-linking reaction was quenched by 0.125M glycine in 1× PBS solution for 5 min under vacuum, followed by three times washes with cold 1× PBS. Samples were then dried briefly, snap-frozen in liquid nitrogen, and ground to a fine powder. The powder was incubated in 30 ml cold Complete Extraction Buffer 1 (with protease inhibitors, 5 mM 2-mercaptoethanol, and 0.1 mM PMSF pre-mixed) at 4 °C (on a rotating wheel) for 30 min. The suspension was successively filtered through 60 μm and 20 μm nylon net filters (Merck Millipore) and centrifuged for 20 min at 4 °C at 1,000× g. The nuclei-containing pellet was washed three times with 5 ml Complete Extraction Buffer 2 (with protease inhibitors and 10 mM 2-mercaptoethanol), one time

with 5 ml Complete Extraction Buffer 3 (containing protease inhibitors and 10 mM 2-mercaptoethanol), then incubated in 800 μl Sonication Buffer (incl. protease inhibitors and 0.1 mM PMSF) for 15 min on ice. Lysate (chromatin) was sheared in the sonication tube (250 μl per tube) with the Bioruptor® Pico (Diagenode) for 8 cycles with the settings 30 s ON / 30 s OFF on ice. The sonicated chromatin from the same replicate was then pooled into a Protein LoBind Tube (Eppendorf) and centrifuged for 10 min at 4 °C at 12,000× g to obtain around 200bp fragments in the supernatant. Sheared chromatin concentration was determined with a Qubit™ dsDNA HS assay (Invitrogen). The shearing efficiency was assessed by gel electrophoresis of de-crosslinked chromatin fragments.

DiaMag protein A-coated magnetic beads were linked to antibodies (Anti-GFP or IgG) in a rotator for 5 hours at 4 °C. Before and after the co-incubation, beads were washed three times with a cold 1× ChIP Dilution Buffer. After a 1:5 dilution with cold 1× ChIP Dilution Buffer (supplemented with protease inhibitors), the sheared chromatin mentioned above was incubated with the antibody-coated beads overnight in a Protein LoBind Tube (Eppendorf) on a rotating wheel at 4°C after a small aliquot (1%) was reserved as the input control. The beads were then sequentially washed with wash buffers 1, 2, 3, and 4 before being collected in a DNA LoBind Tube (Eppendorf) in Elution Buffer 1. After a 30 min room temperature incubation, a brief vortex, and a short spin, the immunocomplexes were collected into new DNA LoBind tubes and mixed with 4% (v/v) Elution Buffer 2. The input control was diluted with Elution Buffer 1 before being mixed with 4% (v/v) Elution Buffer 2 in parallel. The samples were then de-crosslinked at 65°C overnight. Afterwards, chromatin samples were treated with 1 μl RNase cocktail (Invitrogen) at 37°C for one hour, digested by 2 μl proteinase K (Invitrogen) at 65°C for 5 hours and recovered by ChIP DNA clean & concentrator kit (D5205, ZYMO Research) according to manufacturer's instructions.

The recovered DNA was quantified with the Qubit™ dsDNA HS assay and diluted accordingly (about 1:5), then was used as template for qPCR assay as mentioned above. All primers (see Table S1) were evaluated for their amplification efficiencies (90% - 105%). ChIP-qPCR results were normalized for technical variation, including the amount of input chromatin, the efficiency of immunoprecipitation, and variation in DNA recovery. We exploited the Percent Input Method because it normalizes both background levels and input chromatin compared to the Fold Enrichment Normalization, which only considers the negative antibody control. The ChIP efficiency was calculated as follows:

$$\%_{input} = 2^{-\Delta Ct_{normalized\ ChIP}}$$

where,

$$\Delta Ct_{normalized\ ChIP} = Ct_{ChIP} - (Ct_{input} - \log_2 d)$$

d, dilution factor of the input sample, which is 100 in our case as our starting input fraction is 1%. That means 6.644 ($\log_2 100$) cycles should be subtracted from the input Ct value for ΔCt calculation. The ChIP efficiencies of the experiment and two different control (control 1, IgG control; control 2, plant control) groups were then plotted and statistically tested in R.

To avoid potential contamination, we carried out ChIP experiments with pipette tips that featured an inert, hydrophobic aerosol barrier inside and were certified RNase/DNase-free, DNA and PCR inhibitor-free, and non-pyrogenic (Santa Cruz Biotechnology). Low-binding tips with leak-proof tops were used to maximize the preciseness of pipetting, as mentioned in qPCR methods. Protein/DNA LoBind Tubes (Eppendorf) were used in certain steps to minimize sample retention on tubes.

FEM modelling

For computational simulation of strain-based cell growth, the MorphoMechanX software was used.[119–121] Model templates of 2D Voronoi cells were created from equally spaced point clouds using the CellMaker Add-On in MorphoDynamX. Two meshes with polygonal cells in different sizes were made (Figure S7I): for the "large cells" template, polygonal cells have approximately the same mean size of blade cells in leaf1 at 2DAI, which corresponds to the "proliferation burst" population at its onset, while the "small cells" template corresponds roughly in cell size to the equivalent cell population in leaf8 at 2DAI. To assess the effects of high proliferation in leaf1, we applied the cell division process to 30% of the largest cells in the "large cells" template, generating an additional template ("large cells + division", Figure S7I). These divisions were introduced by the shortest wall rule and the new cell walls were pinched (factor 0.2) to create more realistic daughter cells. The 2D Voronoi meshes were then extruded (depth 4 μm) to create hollow volumetric cells, which were then triangulated and modelled with three node membrane elements (Figure S7H).[119]

The cell periclinal walls were assigned isotropic, averagely stiff, material properties (Saint Venant-Kirchoff material law), while the anticlinal walls were assigned the same material law, but anisotropic, very stiff in the anticlinal direction to prevent unnatural growth along the cell depth for epidermal cells and softer in the periclinal direction, to allow cell growth. Templates were then pressurized to the same turgor pressure for all cells. The parameters used were as follows:

Parameter	Symbol	Value
All simulations		
Thickness (all walls)	t	1 μm
Pressure	P	0.5 MPa
Poisson ratio	ν	0.3
Strain Based Growth Coefficient	*Kstrain*	1

(Continued on next page)

Continued

Parameter	Symbol	Value
Strain Growth Threshold	$\epsilon thresh$	1.0E-03
Growth Step increment	*dt*	0.5
Average mesh element size (longest edge)		1.5 μm
Convergence tolerance	tol	3.0E-03
Periclinal walls Young's modulus	*E*	100 MPa
Anticlinal walls Young's moduli	*Eiso*	10 MPa
	Efiber	1000 MPa

The wall thickness was constant at 1μm, although the same result would be obtained with different thicknesses by adjusting the Young's modulus accordingly. The bottom of the template was assigned Dirichlet boundary conditions by fixing the *z* direction to simulate attachment to internal tissue.

The growth rule assigned was a homogeneous turgor-driven strain-based growth, where each mesh triangle grows proportionally (in amount and direction) to its elastic strain, provided it exceeds the growth strain threshold.[122] After the initial pressurization and mechanical equilibrium computation, the growth simulation occurs in an iterative loop as follows: (i) a growth step, which grows the mesh elements based on the strain accumulated after mechanical equilibrium, is performed, (ii) new mechanical equilibrium is computed. All templates were grown for 50 steps in the simulation. After the simulation, the relevant cellular data (cell area and growth) was exported to CSV files for further analysis in R. For the analysis, cells at the boundary of the template were excluded.

QUANTIFICATION AND STATISTICAL ANALYSES

Quantifications were performed unbiasedly for all experiments. Data were analyzed and visualized by R with the required packages. Cellular growth in leaf development was quantified with independent replicates. Representative samples were determined with uniform standards, including the integrities of samples and imaging periods (time-lapse series) and the distance to the all-sample regression measured by RMSE (Root Mean Square Error). The intact sample with the lowest RMSE and the longest imaging period among biological replicates was chosen as the representative of a group (leaf growth pattern) and visualized by heatmaps.

Data size (e.g., numbers of samples and biological replicates), distribution, and statistical analyses (e.g., data summary with mean ± SE/SD or 95% confidence interval, significance tests for comparisons) were plotted and indicated. Data distribution was also statistically assessed (e.g., distribution visualization with density plot and quantile-quantile plot, normality and homogeneity tests with the Shapiro-Wilk test and Levene's or Bartlett's test, respectively). Once normal data distribution and variance equality were confirmed, parametric tests were performed for comparisons; otherwise, non-parametric tests were used. *p*-values < 0.05 were considered significant differences.

For parametric tests, the two-tailed unpaired Student's *t*-test was used for pairwise comparisons (e.g., Figure 5C); one-way ANOVA (ANalysis Of VAriance) was employed for multiple comparisons, followed by a post hoc Tukey's HSD (honestly significant difference) test to determine the differences among groups (e.g., Figures 5A and 5E); when two variables/factors were involved, e.g., in (Figures 1N and S2E), two-way ANOVA was applied to assess the main effect of each independent variable and their interaction. For leaf geometrical measures at different leaf nodes (covariate) in different genotypes (categorical variable), ANCOVA (ANalysis of COVAriance) was used to determine the rate (slope) of leaf heteroblasty among genotypes (e.g., Figure S2D); post hoc Tukey's HSD was used to test the differences among genotypes (Figure 6A).

For non-parametric tests, Welch's unequal variances *t*-test was used for pairwise comparisons (e.g., Figure 1B); and the Kruskal-Wallis test was used for multiple comparisons, followed by post hoc Wilcoxon Rank Sum pairwise tests with Benjamini-Hochberg (BH or alias FDR) *p*-value adjustment (e.g., Figures 2A, 2F, and 2H).

The empirical cumulative distribution function was exploited for the enrichment analysis of the SPL9-binding site (GTAC) in *CYCD3* promoters (Figure S6D).

Regarding regressions, a cubic polynomial (polynomial degree at three) was used for growth alignment in most cases (e.g., Figures 2D and 4B) unless indicated (e.g., local regression in Figures 1D and 1G), because it was sufficient to capture the general curvilinear trends in the data without overfitting.[33] For correlation analyses (e.g., Figures 2H, S2D, S3P1–S3Q5, and S7K), linear regression was performed, with corresponding equations of the forms (intercepts and slopes) and coefficients annotated. The 95% confidence interval was calculated and visualized by shading along the corresponding regression lines.